Contents lists available at ScienceDirect

Materials Science & Engineering A

journal homepage: www.elsevier.com/locate/msea

Assessing the efficacy of several impact-based mechanical techniques on fatigue behavior of additive manufactured AlSi10Mg

Erfan Maleki [a,b], Sara Bagherifard [c,*], Okan Unal [d,e], Shuai Shao [a,b], Nima Shamsaei [a,b], Mario Guagliano [c]

[a] National Center for Additive Manufacturing Excellence (NCAME), Auburn University, Auburn, AL, 36849, United States
[b] Department of Mechanical Engineering, Auburn University, Auburn, AL, 36849, United States
[c] Department of Mechanical Engineering, Politecnico di Milano, Milano, 20158, Italy
[d] Department of Mechanical Engineering, Karabuk University, Karabuk, 78050, Turkey
[e] Modern Surface Engineering Laboratory (MSELAB), Karabuk University, Karabuk, 78050, Turkey

ARTICLE INFO

ABSTRACT

Post-processing methods to reduce issues associated with the presence of internal and external anomalies are often necessary for obtaining adequate structural performance for additively manufactured products. However, the choice of the proper post-treatment and the corresponding parameters is still a challenge requiring adaption to the material type, geometry, size and undeniably costs. In this study, four different pure impact-based mechanical operations involving ultrasonic nanocrystal surface modification (UNSM), ultrasonic shot peening (USSP), severe shot peening (SSP), and severe vibratory peening (SVP) to investigate their efficacy on the fatigue behavior of hourglass AlSi10Mg specimens manufactured via laser powder bed fusion (LPBF) were considered. Experimental characterizations involving microstructural approach, porosity level and surface texture, hardness and residual stresses measurements, as well as tensile and fatigue testing, were conducted. The results exhibited considerable improvement in mechanical/physical performances leading to substantially enhanced fatigue performance of the mechanically treated specimens. Based on a cost-performance analysis, it was found that UNSM, while having reasonable cost, presented considerable improvement on fatigue behavior.

1. Introduction

Laser powder bed fusion (LPBF), a complex and influential additive manufacturing (AM) process, provides the manufactured parts with intrinsic features and dimensions. However, due to the complex manufacturing process including layer by layer melting and rapid solidification (high cooling rates of $\sim 10^6$ K/s [1,2]), these materials are majorly affected by multiple volumetric and surface anomalies [3–5]. In as-built configuration, these materials represent inhomogeneous microstructure [6], several types of volumetric defects (due to gas entrapment or joining failure, etc.) [7,8], hazardous residual stress [9, 10], and surface macro/micro distortions [11]. Completely unmelted powder aggregates, spatters and powder metal defects are known as the main sources of surface imperfections [12–15]. These defects potentially lower the performance of LPBF materials by means of wear, scratch and corrosion resistance as well as their fatigue behavior [16–21]. In particular, surface imperfections behaving like local stress concentration regions lead to early crack nucleation and thus fatigue failure when subjected to cyclic loading [22,23]. Therefore, post-processing methods are being widely evaluated in the AM sector as they are essential to address these challenges [24,25].

Heat treatment (HT) can modulate some of the internal defects; in particular, homogenizing the microstructures and removing its anisotropy, besides releasing the intrinsic tensile residual stresses (TRS). Ductility of the LPBF materials can also be improved with HT [26,27], which may lead to enhanced fatigue behavior, specifically in the low-cycle fatigue regime [28,29]. Hot isostatic pressing (HIP) is also a commonly used post-treatment that besides homogenizing the microstructure of AM materials, can also reduce their porosity. This process simultaneously subjects the component to elevated temperature and isostatic gas pressure in a high-pressure containment vessel [30–32].

Among non-subtractive post-processing methods sourced to address the surface inadequacy, impact-based surface treatments have gained considerable attention. This category can include a wide range of treatments, such as shot peening (SP) [33–35], ultrasonic shot peening

Abbreviations

AM	Additive Manufacturing
CRS	Compressive Residual Stresses
CSP	Conventional Shot Peening
ECP	Electro-Chemical Polishing
EL	Elongation To Fracture
HT	Heat Treatment
HIP	Hot Isostatic Pressure
IPF	Inverse Pole Figure
KAM	Kernel Average Misorientation
LP	Laser Polishing
LPBF/LB-PBF	Laser Powder Bed Fusion
LRM	Laser Re-Melting
LSP	Laser Shock Peening
M	Machining
P	Polishing
SB	Sand Blasting
SSP	Severe Shot Peening
SVP	Severe Vibratory Peening
SP	Shot Peening
TRS	Tensile Residual Stresses
UTS	Ultimate Tensile Strength
UNSM	Ultrasonic Nanocrystal Surface Modification
USSP	Ultrasonic Shot Peening
VF	Vibratory Finishing
YS	Yield Strength

(USP) [36], severe vibratory peening (SVP) [37] and ultrasonic nanocrystal surface modification (UNSM) [38–40]. These operations all follow the same concept of mechanically inducing surface plastic deformation; they remove the surface irregularities, homogenize the surface morphology and can induce grain refinement and high compressive residual stresses (CRS) on (and in the vicinity of) the surface [41–45]. However, despite the common physics, these treatments differ in the type of the equipment, have dissimilarities in the range of treatable geometries and require different exposure times.

AlSi10Mg parts can be fabricated by LPBF at bulk volume density without solidification cracks owing to near eutectic composition of this alloy. The occurrence of quite small cellular structure during LPBF process in this alloy offers acceptable combination of ductility and strength [46–50]. Numerous studies have revealed the effect of various post-treatments and mechanical performance of AlSi10Mg manufactured by LPBF. The list of the applied surface post-processing methods (with and without material removal) and the material properties involving surface roughness, residual stress, hardness, corrosion and fatigue behavior are presented in Table 1.

As shown in Table 1, the post-treatments can effectively decrease the surface roughness or modify the surface morphology, enhance the mechanical performance, such as wear and corrosion resistance and improve fatigue behavior. For example, application of USP on LPBF AlSi10Mg with a 17 kHz frequency and a power of 1000 W and an amplitude of 80 μm resulted in remarkable porosity reduction and surface hardening as well as induced high surface CRS compared to the prior stress state, leading to notable corrosion resistance improvement [54]. In another study, SP process applied by Almen intensity, 10A [0.001 inch] and 100% coverage via steel media, led to surface roughness reduction for LPBF AlSi10Mg specimens decreasing R_a from 9.0 to 4.5 μm [58]. The combined effect of reduced surface morphology, surface hardening as well as maximum in depth CRS up to −155 MPa (on the contrary as-built state has 70 MPa tensile stresses), led to remarkable fatigue strength enhancement.

In our prior investigations, we surveyed the impact of multiple post operations of conventional shot peening (CSP) [60,61], SVP [37] and LSP [62] combined with HT on fatigue performance of notched LPBF AlSi10Mg specimens. The results demonstrated noteworthy fatigue life enhancement up to 233, 235 and 243 times better against AB specimen at a stress of 110 MPa via hybrid treatments of HT + CSP, HT + SVP and HT + LSP, respectively. Herein, differentiating from the previous studies, we specifically focus on different peening-based technologies to evaluate their effects when applied at the same energy level, to compare their efficacy, advantages, and limitations. In particular, severe shot peening (SSP), USP, SVP and UNSM are applied individually and combined with HT on LPBF AlSi10Mg specimens. Detailed experiments involving monotonic tensile tests, microstructural characterization, surface morphology and roughness measurements, porosity, hardening and internal residual stresses evaluations and fatigue behavior determination were conducted on all specimens to assess the efficacy of the applied surface post-treatments.

2. Experimental procedures

2.1. Material and specimens preparation

AlSi10Mg powder produced by gas atomization with the nominal size interval of 20–70 μm and average diameter of 50 μm was utilized for manufacturing of LPBF specimens as demonstrated in Fig. 1a. Table 2 presents powder chemical composition. The specimens were produced vertically as illustrated in Fig. 1b via an SLM 500 HL equipment by using Yttrium fiber lasers by a spot diameter of 78 μm and a power of 350 W. The rotation degree of 67° was utilized between the adjacent layers and contouring as depicted in Fig. 1c. The schematic view of the cylindrical hourglass fatigue test specimens is shown in Fig. 1d. In addition, miniature flat tensile test specimens were prepared later by wire cutting out of the fatigue specimens as shown in Fig. 1e. The shape of the miniature specimens follows the specifications presented by Cosa et al. [63] (Fig. 1f). Fig. 1g and h shows the schematic illustration of the manufacturing process of the specimens, layer-by-layer via LPBF technology and the variety of their possible internal and surface anomalies, respectively.

2.2. Post-processing methods

Different impact-based mechanical surface operations involving SSP, USP, SVP and UNSM as well as their combination with HT were applied to hourglass LPBF AlSi10Mg specimens. T6 type thermal treatment was applied to the specimens (merely half of the whole) aiming to homogenize the overall structure and vanish the TRS of the as-built state. T6 HT was applied according to durations and temperature zones demonstrated in the prior work [60], with an initial temperature towards 520 °C, solution based HT for 1 h, water quench for 1 h, subsequent to reaching temperature to 160 °C and aging for 6 h at 160 °C, followed by water quenching.

During the SSP, the surface of the specimen is exposed to shot flow either using high values of Almen intensity (index of deformation capability) or surface coverage (associated with peening duration) as presented in Fig. 2a. In the USP treatment, larger impacting media under an ultrasonic frequency in a peening chamber as depicted in Fig. 2b. The SVP treatment, on the other hand, utilizes high-frequency vibration and thus induces severe plastic deformation as presented in Fig. 2c. Finally, during the UNSM treatment, high frequency elastic waves generated by ultrasonic generator are amplified by a WC horn, which is impacted to the surface of specimen using a defined scanning direction as shown in Fig. 2d. Here, to compare the impact of these mechanical operations on

Table 1

Summary of typical post-processing methods applied on LPBF AlSi10Mg specimens.

Post-processing method	Category[a]	Remarks	Ref.
Laser polishing (LP)	No additional removing operation	• Surface roughness reduction Surface roughness of as-built state: R_a[b] = 8 μm Surface roughness of LP: R_a = 0.25 μm	[51]
Laser shock peening (LSP)	No additional removing operation	• Sub-surface porosity reduction Porosity in as-built state: ~0.87% Porosity after LSP: ~0.02%	[52]
Vibratory finishing (VF)	Additional removing operation	• Surface roughness reduction Surface roughness of as-built state: S_a = 14 μm Surface roughness of VF: S_a = 4 μm	[53]
Ultrasonic shot peening (USP)	No additional removing operation	• Increasing surface hardness Surface microhardness of as-built state: 116 Hv Surface microhardness of USP: 142 Hv • Inducing CRS Surface residual stress of as-built state: 38 MPa Surface residual stress of USP: −155 MPa • Increasing corrosion resistance	[54]
Sand blasting (SB), VF, Machining (M) and Polishing (P)	No additional removing operation for SB and additional removing operation for VF, M and P	• Surface roughness reduction Surface roughness of as-built state: S_a = 15.4 μm Surface roughness after SB: S_a = 8.3 μm Surface roughness after VF: S_a = 2.3 μm Surface roughness after M + P: S_a = 0.5 μm • Increasing fatigue strength Fatigue strength in as-built state: 50–62 MPa Fatigue strength after SB: 152.5 MPa Fatigue strength after VF: 95 MPa Fatigue strength after M + P: 194 MPa	[55]
Laser re-melting (LRM)	No additional removing operation	• Surface roughness reduction Surface roughness in as-built state: R_a = 20.6 μm Surface roughness after SB: R_a = 10.8 μm • Porosity reduction Porosity in as-built state: 0.15 vol% Porosity after LRM: 0.09 vol%	[56]
M, P, electro-chemical polishing (ECP), Shot peening (SP)	Additional removing operation for M, P, ECP and no additional removing operation for SP	• Surface roughness reduction Surface roughness in as-built state: R_a = 8.92 μm Surface roughness after M: R_a = 1.75 μm Surface roughness after M + P: R_a = 0.59 μm Surface roughness after SP: R_a = 4.60 μm	[57]

Table 1 (*continued*)

Post-processing method	Category[a]	Remarks	Ref.
		Surface roughness after SP + P: R_a = 2.15 μm Surface roughness after SP + ECP: R_a = 1.77 μm • Increasing fatigue strength (smooth sample) Fatigue strength of as-built state: 75 MPa Fatigue strength after SP: 105 MPa	
SP and SB	No additional removing operation	• Surface roughness reduction Surface roughness of as-built state: R_a = 9.1 μm Surface roughness after M: R_a = 6.5 μm Surface roughness after SB: R_a = 4.8 μm • Increasing surface hardness Surface microhardness in as-built state: 131 Hv Surface microhardness after SP: 157 Hv Surface microhardness after SB: 145 Hv • Inducing CRS Surface residual stress in as-built state: 49 MPa Surface residual stress after SP: −80 MPa Surface residual stress after SB: −85 MPa • Increasing fatigue strength (Smooth sample) Fatigue strength of as-built state: 50 MPa Fatigue strength after SP: 185 MPa Fatigue strength after SB: 173 MPa	[58]
M, SP	Additional removing operation M and no additional removing operation for SP	• Surface roughness reduction Surface roughness of as-built state: R_a = 6.89 μm Surface roughness after SP: R_a = 5.82 μm Surface roughness after M: R_a 0.22 μm Surface roughness after SP: R_a = 2.05 μm • Increasing surface hardness Surface microhardness in as-built state: 120 Hv Surface microhardness after SP: 154 Hv Surface microhardness after M: 128 Hv Surface microhardness after M + SP: 145 Hv • Inducing CRS Surface residual stress in as-built state: 11 MPa Surface residual stress after SP: −152 MPa Surface residual stress after M: −79 MPa Surface residual stress after M + SP: −140 MPa	[59]
SP	No additional removing operation	• Surface morphology modification	[60]

Table 1 (*continued*)

Post-processing method	Category[a]	Remarks	Ref.
		• Increasing surface hardness Surface microhardness in as-built state: 121 Hv Surface microhardness after SP: 155 Hv • Inducing CRS Surface residual stress in as-built state: −11 MPa Surface residual stress after SP: −83 MPa • Increasing fatigue strength (Notched sample) Fatigue strength in as-built state: 6 MPa Fatigue strength after SP: 92 MPa	
Chemical polishing (CP) and ECP and SP	Additional removing operation for CP and ECP and no additional removing operation for SP	• Surface morphology modification • Surface roughness reduction Surface roughness in as-built state: $R_a = 4.49$ μm Surface roughness after CP: $R_a = 3.19$ μm Surface roughness after ECP: $R_a = 2.96$ μm Surface roughness after SP: $R_a = 4.61$ μm Surface roughness after SP + ECP: $R_a = 3.29$ μm • Increasing fatigue life (notched sample; stress amplitude of 110 MPa) Fatigue life in as-built state: 1.26×10^4 Fatigue life after CP: 1.41×10^5 Fatigue life after ECP: 2.15×10^5 Fatigue life after SP: 1.19×10^6 Fatigue life after SP + ECP: 3.67×10^6	[61]

***Sa: arithmetical mean height of an area.

[a] Based on the classification of post operations of AM products presented in Ref. [25].

[b] R_a: arithmetical mean of height.

specimens, equal level of kinetic energy was used for all operations by specifying the same range of Almen intensity that is majorly employed among SP operations. Each treatment was operated on an Almen strip A to reach Almen intensities of 10–12A [0.001 inch], by measuring the arc heights of the strips. Fig. 2e presents the measured arc heights in different exposure times for each considered treatment. The detail of parameters of the applied treatments are listed in Tables 3–6. Overall, a total of 10 sets of specimens involving AB, AB + SSP, AB + USP, AB + SVP, AB + UNSM, AB + HT, AB + HT + SSP, AB + HT + USP, AB + HT + SVP and AB + HT + UNSM were prepared in this study to examine the mere and hybrid influence of several post-processing treatments.

2.3. Experimental characterizations

Microstructural analyses were performed by using an optical microscope (Nikon Eclipse LV150NL) and a Zeiss Sigma 500 VP scanning electron microscope (SEM) equipped with electron back-scatter diffraction (EBSD) and energy dispersive spectrometry (EDS) detectors. EBSD results were processed by AZtecHKL software. Considering build direction, the specimens were cut through cross-sections and were

etched using Keller's reagent for 20 s. In addition, XRD analyses were carried out using Rigaku SmartLab XRD equipment with CuKα radiation, with around 40 kV voltage, and 30 mA current. The average width of at half height (FWHM) parameter was evaluated using Gaussian approach. Afterwards, the crystallite size was calculated via Williamson-Hall relation described in Ref. [64].

Porosity measurments were conducted via X-ray computed tomography (Nikon XTH 225ST micro-CT) at 190 kV voltage, 40 μA current and 3900 ms exposure time. Specimens' surface morphology was analyzed using a Zeiss EVO50 SEM. Roughness investigation around the highest stress concentration zone (middle of the specimens) was conducted via Alicona Infinite Focus microscope. ISO 25178-2 standard [60, 65] was followed to obtain the values of roughness parameters of arithmetic roughness average of the surface (R_a) and the root mean square of the surface roughness (R_q). Microhardness tests were carried out on polished longitudinal *yz*-plane (considering *z* axis for build direction) via Leica WMHT30A equipment (microvickers) with the load of 0.25 N and the load application duration of 15 s considering 50 μm spacing between indentations. Three paths were used on each specimen from surface through 740 μm interior. X-ray diffraction (XRD) was performed to obtain the variation of residual stress using AST X-Stress 3000 CrKα radiated XRD equipment. Measurements were performed from surface towards the inside of the specimen for a depth of 700 μm to assess the perpendicular path with respect to the build direction. ECP was employed for thinner layer removal in each step using acetic (94%) and perchloric acid (6%) solution at 40 V.

The tensile tests were performed via electromechanical universal testing equipment of MTS QTEST/100 at an operation speed of 1.5 mm/min at 25 °C using a miniature MTS 632.29 extensometer with the gage length of 5 mm. The utilized extensometer had the strain measurement capacity of −10%–30%, which was extensively convenient for the subsize tensile test specimens for dilatometry. Fatigue behavior of specimens was assessed using an Italsigma rotating bending fatigue test equipment at a constant stress of 110 MPa, the stress ratio of R = −1 and the angular speed of 2500 rpm. The run-out limit was determined as 1.5×10^7 cycles. Three specimens were tested for each condition and the average fatigue lives were used for all comparisons. In addition, fractography assessment was conducted to the failed specimen by using Zeiss EVO50 SEM.

3. Results

3.1. Tensile behavior

Fig. 3a and b shows the comparison of stress-strain curves for all the specimens. Histograms in Fig. 3c and d shows the average data of the three tested specimens. Tensile test outputs revealed a considerable distinction between the quasi-static tensile properties pre and post HT (AB vs. AB + HT) demonstrating a notable enhancement of elongation to fracture (EL) along with reduction of yield (YS) and ultimate tensile strength (UTS). EL was raised from 3% up to 14% after HT, however, YS and UTS diminished from 273 to 385 MPa down to 201 and 264 MPa, respectively.

The mechanical surface treatments, on the other hand, increased both YS and UTS while slightly diminishing the EL, as summarized in Table 7. As similarly reported for conventional and AM materials subjected to mechanical surface treatments, changes in YS were more significant than that of the UTS [66–70]. This strengthening effect induced by the peening based surface treatments can be associated with surface grain refinement and the presence of CRS [71].

3.2. Microstructural analyses

Fig. 4a depicts the optical microscopy (OM) investigations of AB/AB + HT specimens in both transverse and longitudinal cross-sections. In the AB specimen inhomogeneous microstructure can be observed with
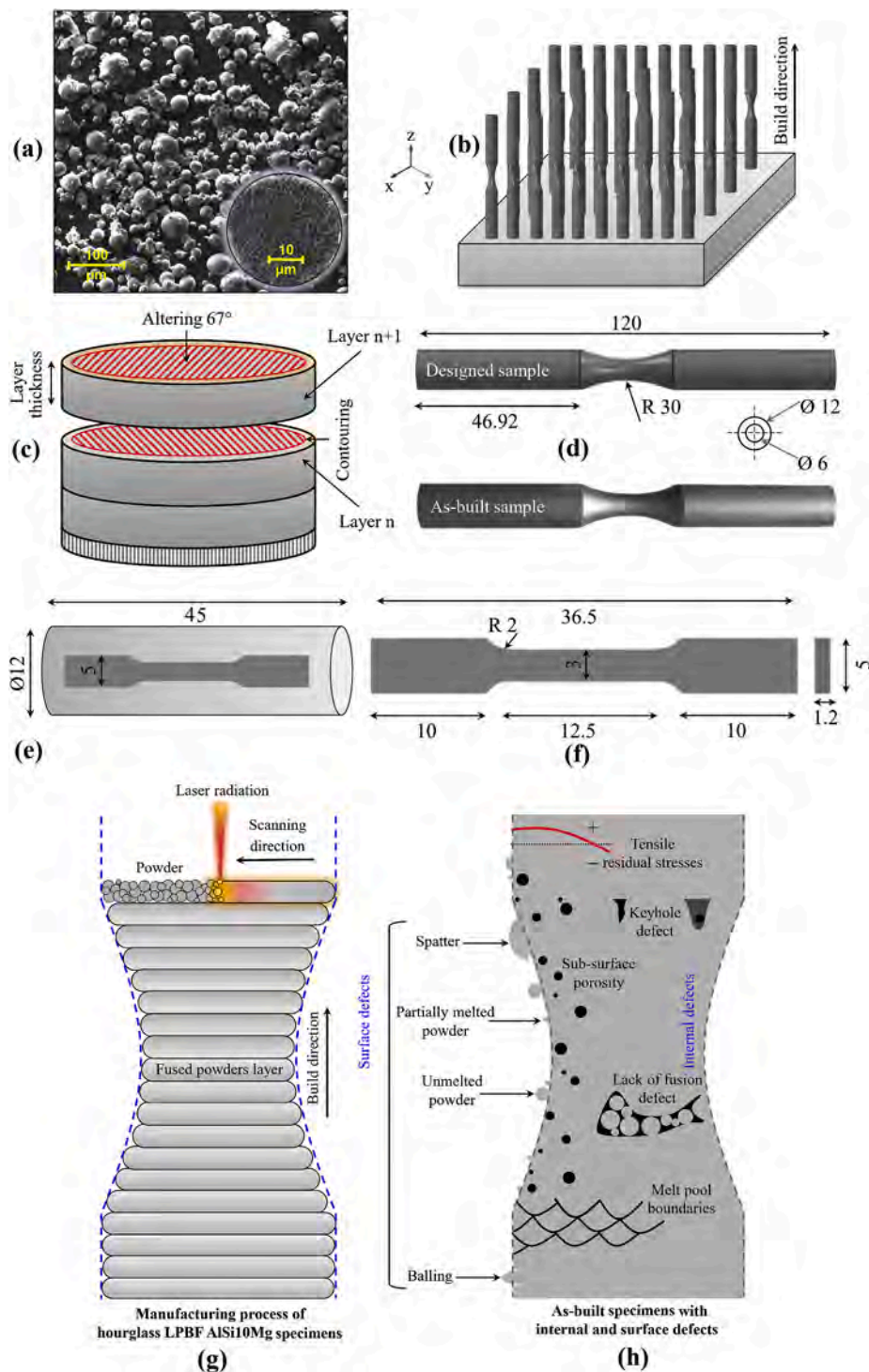
Fig. 1. (a) Morphology of the employed gas atomized AlSi10Mg powder and corresponding microstructure. (b) Cylindrical specimens fabricated along vertical build direction. (c) Schematic view of 67° rotation between adjacent layers for contouring. (d) Shape of the cylindrical hourglass fatigue test specimens. (e) Preparation of miniature tensile test specimens by wire cutting of the cylindrical parts of the fatigue test specimens and (f) shape and dimensions of the subsize tensile test specimens. (g) Schematic illustration of the manufacturing stages of the hourglass specimens layer-by-layer via LPBF technology, and (h) the possible internal and surface anomalies of these specimens. All dimensions are in mm.

Table 2
AlSi10Mg powder chemical composition.

Element	Al	Si	Fe	Cu	Mn	Mg	Zn	Ti	Ni	Pb	Sn
AlSiMg10 (wt%)	Balance	9.87	0.07	<0.01	0.002	0.35	<0.01	<0.01	<0.01	<0.01	<0.01

tracks of melt pool boundaries and hatching lines. While, in the AB + HT specimen, the boundaries of melt pool and hatch like traces are less noticeable resulting in considerable homogenized microstructure. Only few faded melt pool boundaries persist, which is likely phenomena in LPBF AlSi10Mg heat treated at temperatures around 240–450 °C [72]. This homogenization leads to enhanced ductility after HT.

EBSD analyses were also performed on both AB/AB + HT specimens to obtain the maps of grain boundaries, inverse pole figure, grain size
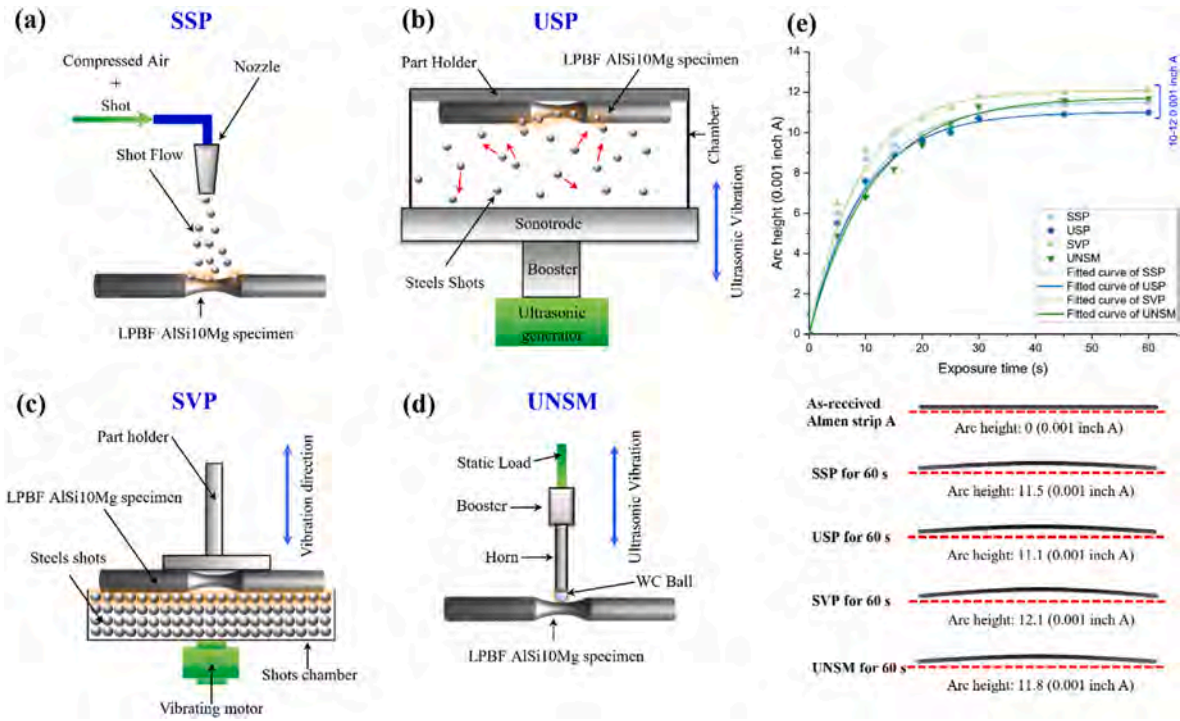
Fig. 2. Schematic illustration of different mechanical surface treatments including (a) SSP, (b) USP, (c) SVP and (d) UNSM, as well as (e) measured arc heights in different exposure times for all the considered treatments resulting in Almen intensity of 10–12 A [0.001 inch] in all of them.

Table 3
Parameters of the SSP treatment applied to the LPBF AlSi10Mg specimens.

Treatment	Shot material	Shot hardness (HRC)	Shot diameter (mm)	Projection pressure (Bar)	Peening duration (s)	Surface coverage (%)	Incident distance (mm)
SSP	Steel	48–50	0.43	3	1500	1000	120

Table 4
Parameters of USP treatment applied to the LPBF AlSi10Mg specimens.

Treatment	Shot material	Shot hardness (HRC)	Shot diameter (mm)	Shot number	Amplitude (μm)	Peening duration (s)	Incident distance (mm)
USP	Steel	48–50	0.58	250	50	300	50

Table 5
Parameters of SVP treatment parameters for the LPBF AlSi10Mg specimens.

Treatment	Shot material	Shot hardness (HRC)	Frequency (Hz)	Shot type	Shot diameter (mm)	Lubrication state	Peening duration (min)
SVP	Steel	52	50	100Cr6	1	Dry	30

Table 6
Parameters of the UNSM treatment applied to the LPBF AlSi10Mg specimens.

Treatment	Impacting material	Frequency (kHz)	Amplitude (μm)	Linear speed (mm/min)	Static load (N)	Path Interval (μm)	Ball diameter (mm)
UNSM	WC	20	30	2000	50	65	2.5

distributions and strain contouring. Fig. 4b illustrates the grain boundary zones of both AB/AB + HT specimens with different misorientations of 2°< (green lines) and 5°< (black lines). Formation of finer equiaxed grains around the boundaries of melt pool (in both xy-plane and yz-plane) as well as epitaxial growth of columnar grains (in yz-plane), which is a common phenomenon in LPBF metallic materials, can be noted [73]. In addition, in the semi-visible melt pool boundaries of AB + HT condition, the elongation of columnar grains have also been reported by previous studies [74].

Fig. 4c indicates the inverse pole figure (IPF) maps and the oriented crystallography of the both AB/AB + HT specimens. The outputs exhibit random orientation of the grains with domination of (001) orientation in xy-planes which is parallel to the build direction in the longitudinal planes; this is because of the solidification along the direction of the heat transfer and the resulting epitaxial grain growth [75–78].

Fig. 4d demonstrates the corresponding grain size distribution maps exhibiting grain growth after HT. The mean grain areas of 2.8 and 44.8 μm^2 were estimated on xy/yz planes for AB specimens, respectively.
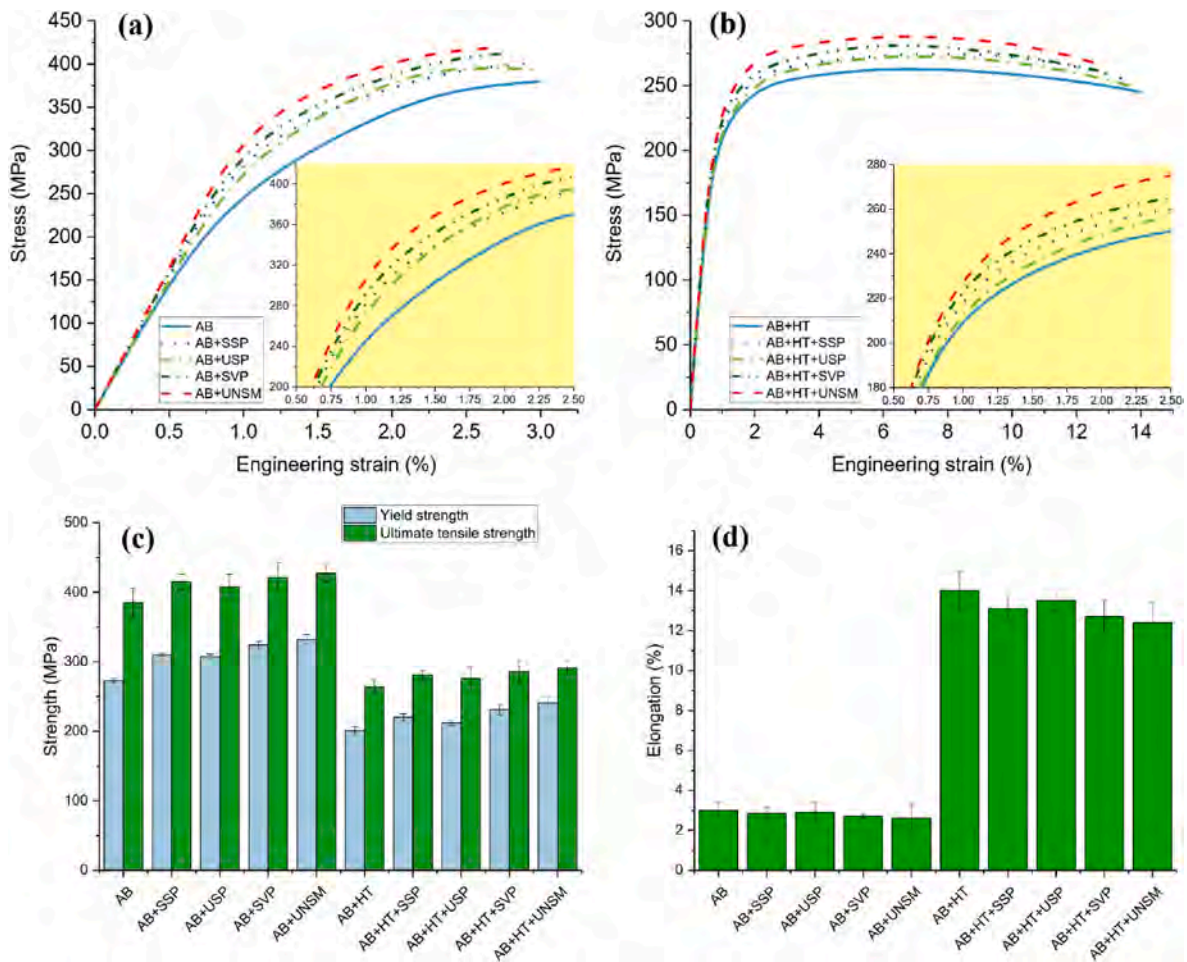
Fig. 3. Comparison of stress-strain curves of all sets of post-processed specimens in (a) as-built and (b) heat treated conditions. The average data of the three specimens tested for each set, in terms of (c) YS and UTS and (d) EL.

Table 7
Variation of tensile properties after surface post-processing in as-built and heat treated conditions.

	YS increase compared to the AB state (%)	UTS increase compared to the AB state (%)	EL reduction compared to the AB state (%)	YS increase compared to the HT state (%)	UTS increase compared to the HT state (%)	EL reduction compared to the HT state (%)
After SSP	13.55	10.98	−0.05	6.95	6.22	−0.32
After USP	12.45	8.42	−0.03	4.02	4.39	−0.18
After SVP	18.68	13.18	−0.10	10.98	8.05	−0.47
After UNSM	21.61	15.38	−0.13	14.65	9.89	−0.58

While, in the AB + HT specimens, elongated grains with larger size were measured with mean grain areas of 5.7 and 53.3 μm^2 on xy and yz planes, respectively. The obtained values of mean grain sizes are compatible with the prior works [79–81].

Strain contouring maps that can be used as an index of plastic strain variations were obtained for AB/AB + HT specimens as revealed in Fig. 4e. Strain contouring reveals local plastic strain by interpretation of the inferred lattice distortion and dislocation density [82,83]. The results reveal that effective strains are located onto the melt pool regions where the density of equiaxed grains is higher mainly where the boundaries overlap. In addition, due to the significant homogenization of microstructure after HT as well strain relief, a lower maximum localized strain of 3 was obtained for AB + HT specimen compared to the AB specimen with a maximum strain of 3.5.

Surface layer of the specimens subjected to the peening-based treatments was assessed by EBSD analyses on the transverse cross-section concentrating on a scan area of 30×150 μm^2. Fig. 5 depicts IPF-Z, dynamic recrystallization (DR) intensity, kernel average misorientation (KAM) and strain contour (SC) maps all together. IPF-Z maps prove the coarsening of grains from nano-size in the outmost surface towards the core in pure mechanically operated specimens for both AB and HT conditions. It should be noted that the black fields in IPF-Z figures are related to the nanosized grains with an approximate size of 100 nm that were too small to be detected by using the allowable step size. Recrystallization maps indicate the level of mechanical deformation on the grains by using color mapping; severely deformed grains around the top surface are shown with concentrated red color. It is noticeable that the deformation density gradually decreases as they are
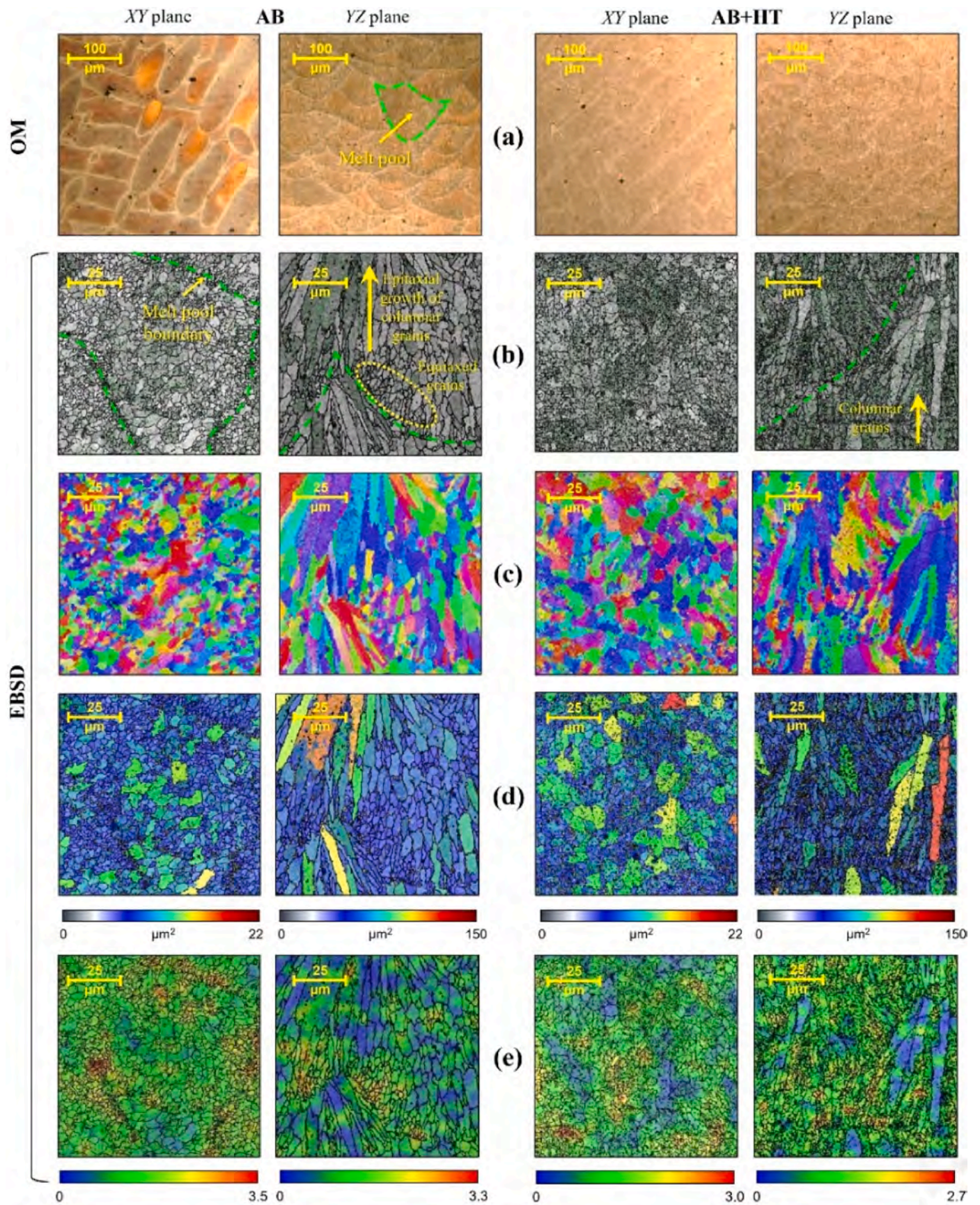
Fig. 4. Microstructural characterization results in both transversal and longitudinal cross-sections for as-built (2 left columns) and heat treated (2 right columns) states obtained by (a) OM investigations and EBSD analyses by means of (b) grain boundaries, (c) IPF, (d) grain size distributions and (e) strain contouring maps.
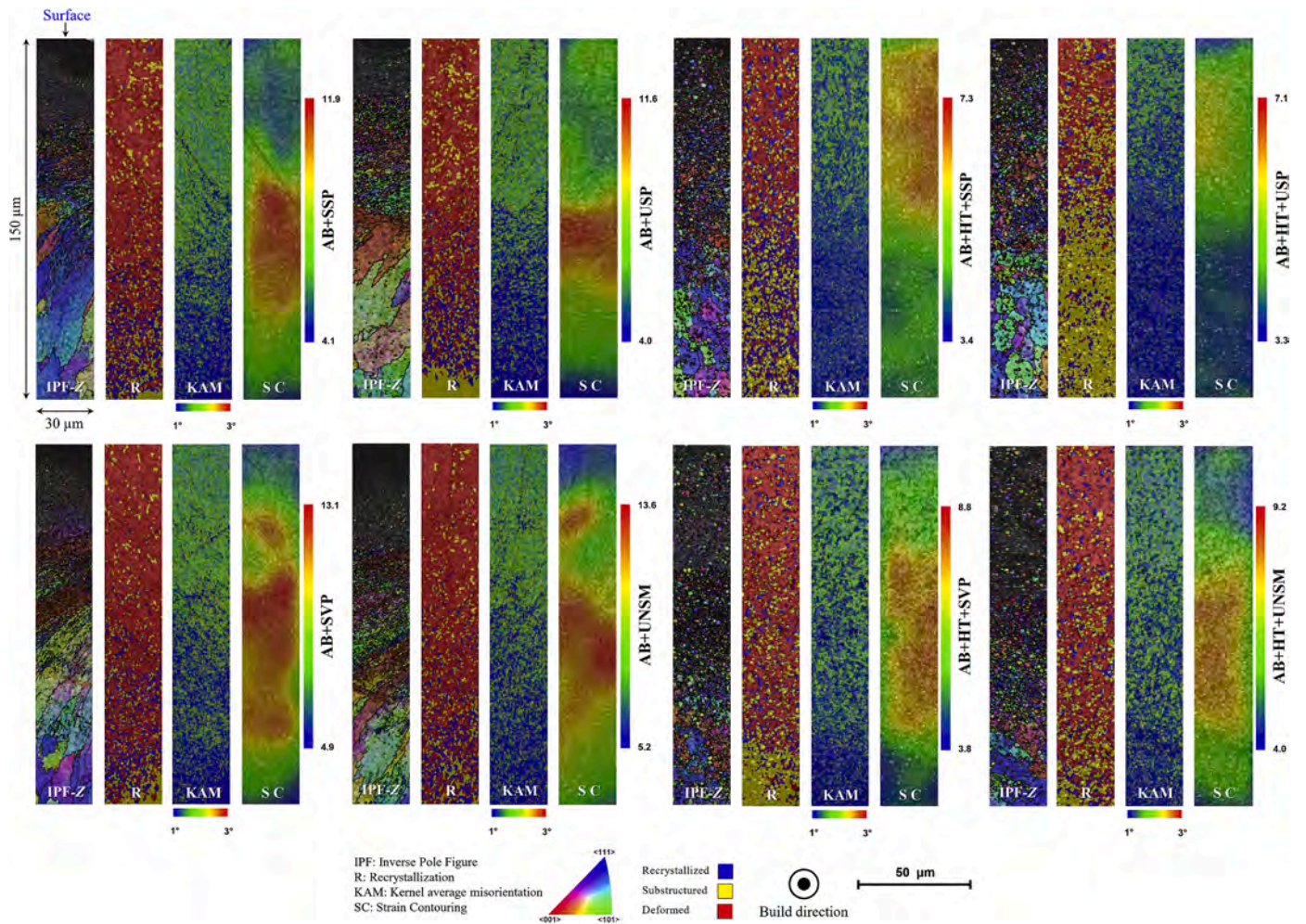
Fig. 5. EBSD results of IPF-Z, DR, KAM and SC maps in the single step treatments of AB + SSP, AB + USP, AB + SVP and AB + UNSM, as well as hybrid treatments of AB + HT + SSP, AB + HT + USP, AB + HT + SVP and AB + HT + UNSM.

replaced with sub-structured (yellow phase) and recrystallized (blue phase) grains towards the interior. The fraction of these three phases varies among the specimens due to the different impacting approach of the surface treatments as well as the initial differences of strength in the as-built and HT conditions.

KAM maps that reflect the variations of applied plastic deformation and cold working [84–86], indicate the highest values in the surface outmost zone, which gradually decreases towards the center. The
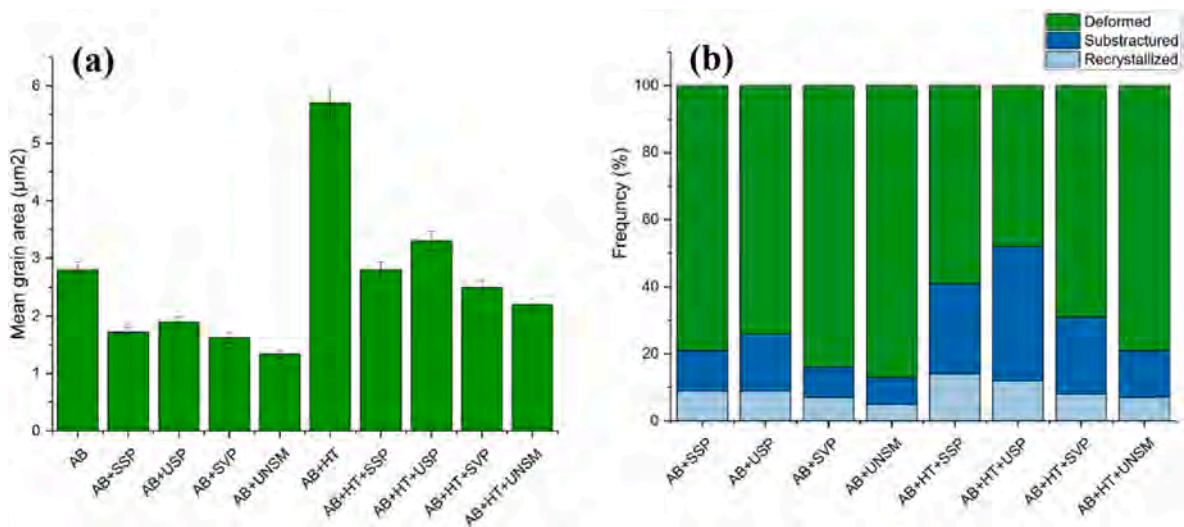

Fig. 6. Quantitative outputs of (a) mean grain area and (b) relative frequency of recrystallized, substructured and severely deformed grains detected by EBSD around the outmost layer.
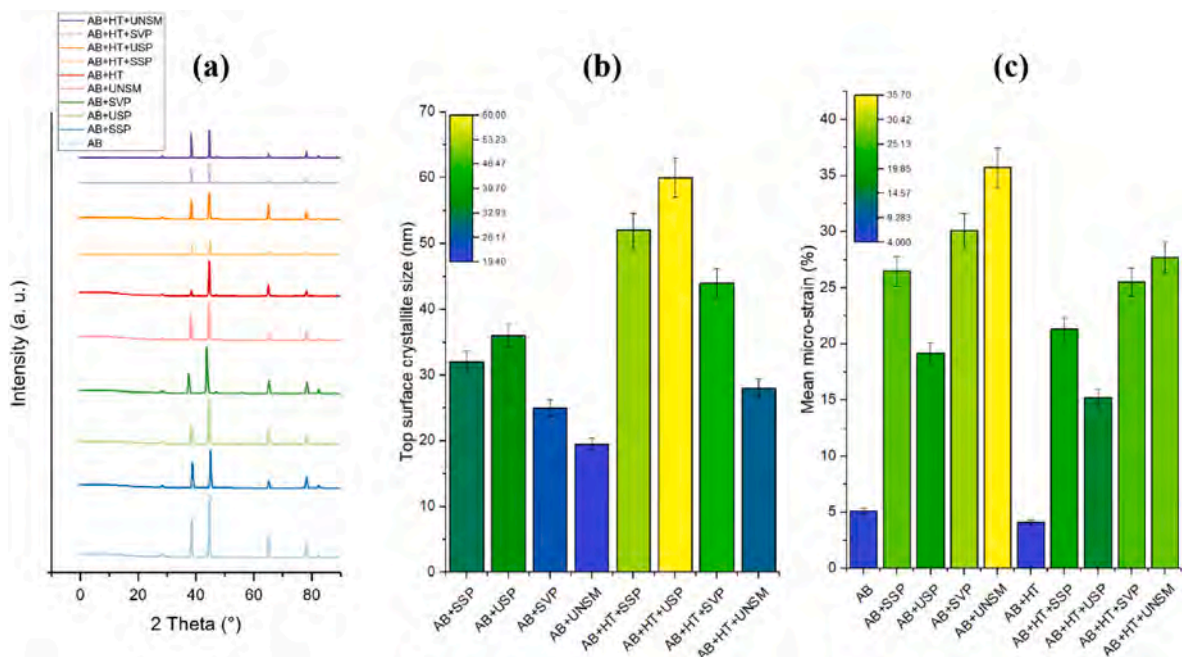
Fig. 7. (a) XRD patterns of the sets of specimens, (b) surface crystallites size and (c) micro-strains obtained by XRD analyses.
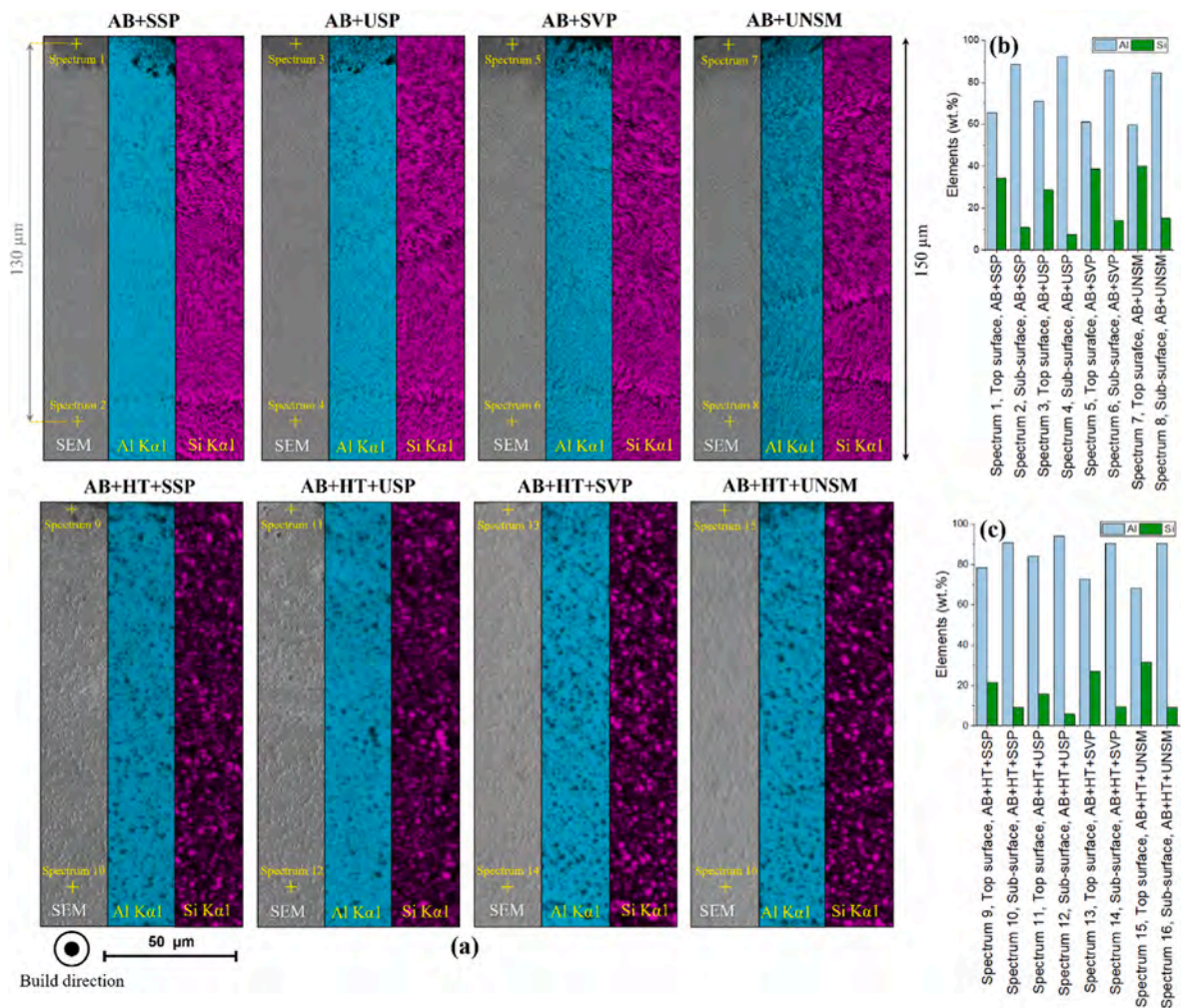

Fig. 8. (a) The obtained EDS maps and the spectrum points for treated specimens; EDS point analysis in the outmost layer for surface treated specimens (b) without and (c) with HT.
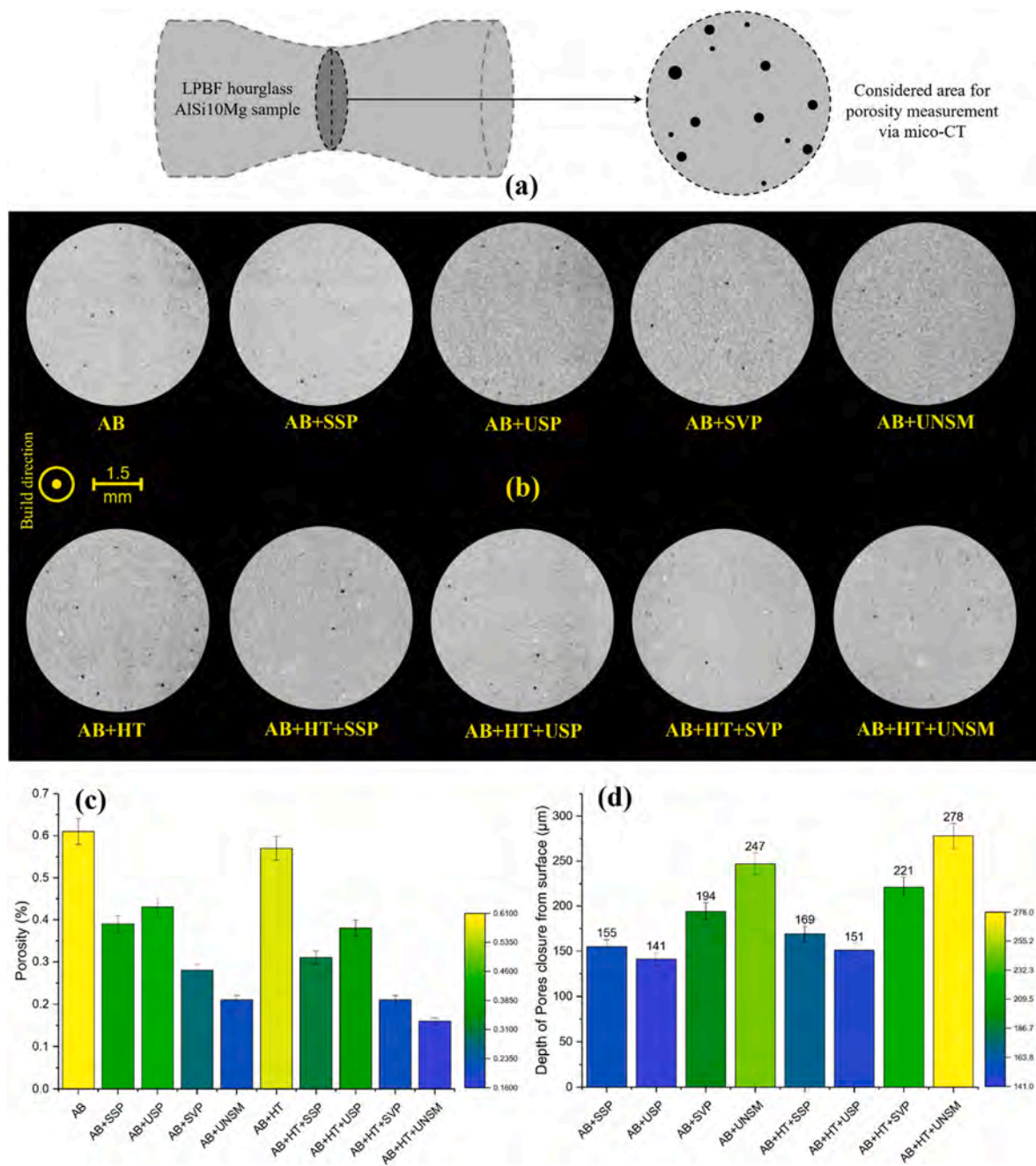
Fig. 9. (a) Mid-section scanned area for porosity measurement by X-ray computed tomography, (b) micro-CT images in transverse sections of the specimens, quantitative data of (b) mean porosities for all sets of specimens and (c) pore closure depth measured from the outmost zone in the mechanically surface treated specimens.

maximum KAM outputs were identified in certain regions with severe plastically deformed grain fields. The results reveal that specimens treated with UNSM had the highest average KAM values followed by SVP, SSP and USP, respectively, in both AB and HT conditions. In particular, mean KAM values of 1.77, 1.61, 1.87, 1.93, 1.26, 1.11, 1.52 and 1.67° were accomplished for AB + SSP, AB + USP, AB + SVP, AB + UNSM, AB + HT + SSP, AB + HT + USP, AB + HT + SVP and AB + HT + UNSM specimens, respectively. Furthermore, the high-KAM depths, corresponding to about 2°, compared to that of low-KAM values, corresponding to about 1°, indicates a good agreement with the depth of refined grains in the IPF-*Z* maps.

Strain contouring maps demonstrate that the highest plastic strains were induced in the specimens treated with UNSM followed by SVP, SSP and USP, respectively. The max. localized plastic strains of 11.9, 11.6,

13.1, 13.6, 7.3, 7.1, 8.8 and 9.2 were determined for AB + SSP, AB + USP, AB + SVP, AB + UNSM, AB + HT + SSP, AB + HT + USP, AB + HT + SVP and AB + HT + UNSM parts, respectively. It has to be mentioned that the max. plastic strains were located just below the surface as is common in the mechanically surface treated materials [87–89]. The results of KAM and strain contouring maps confirm that the applied surface treatments led to lower strain on the HT sets owing to better ductility compared with the sets with initial AB condition.

Quantitative grains size analysis based on EBSD data, shown in Fig. 6a, demonstrates mean grain size reduction in the considered scan area in the surface treated specimens. Mean grain areas of 1.7, 1.8, 1.6, 1.3, 2.8, 3.3, 2.5 and 2.2 μm² were measured for AB + SSP, AB + USP, AB + SVP, AB + UNSM, AB + HT + SSP, AB + HT + USP, AB + HT + SVP and AB + HT + UNSM specimens, respectively. UNSM was shown to be
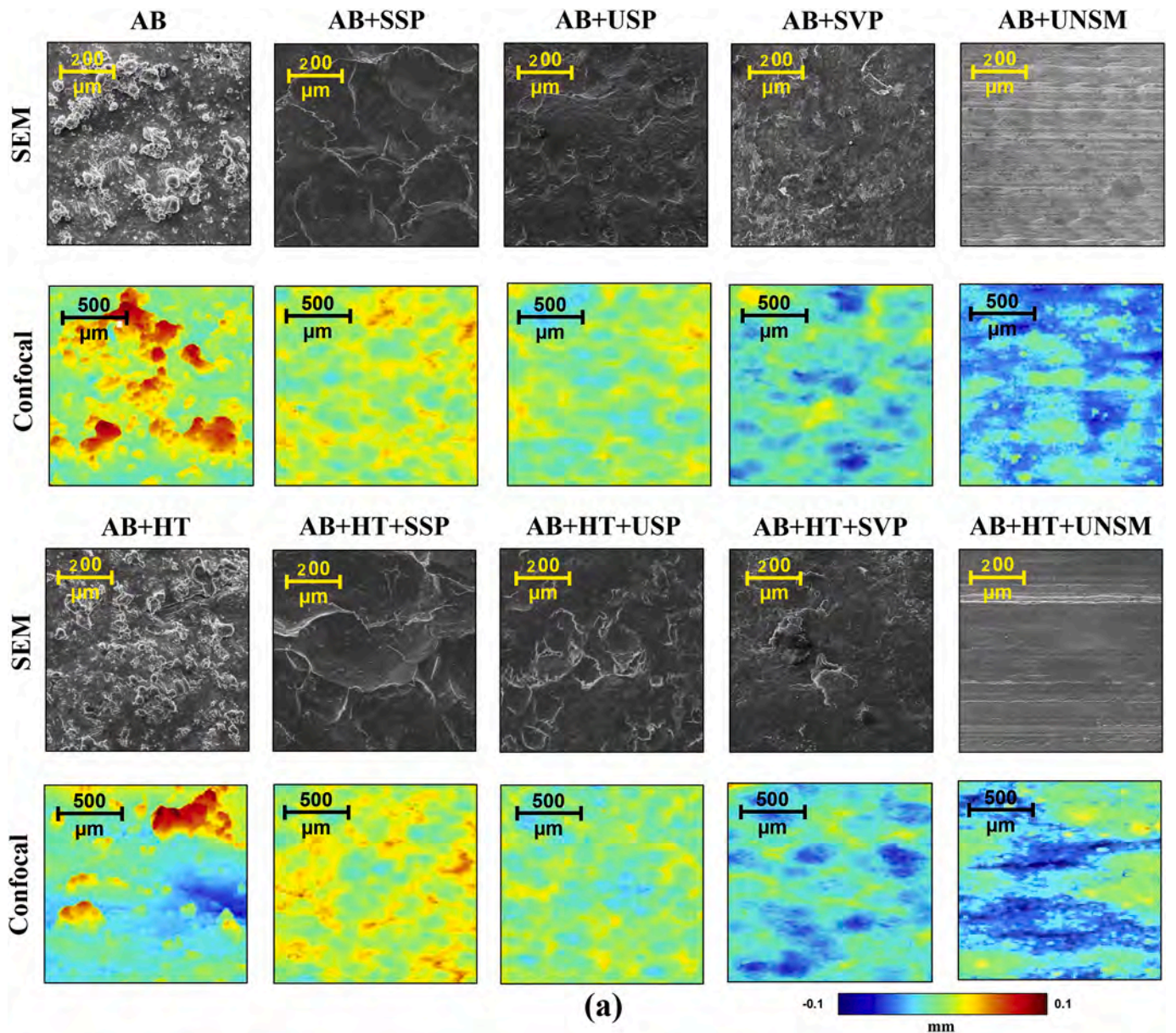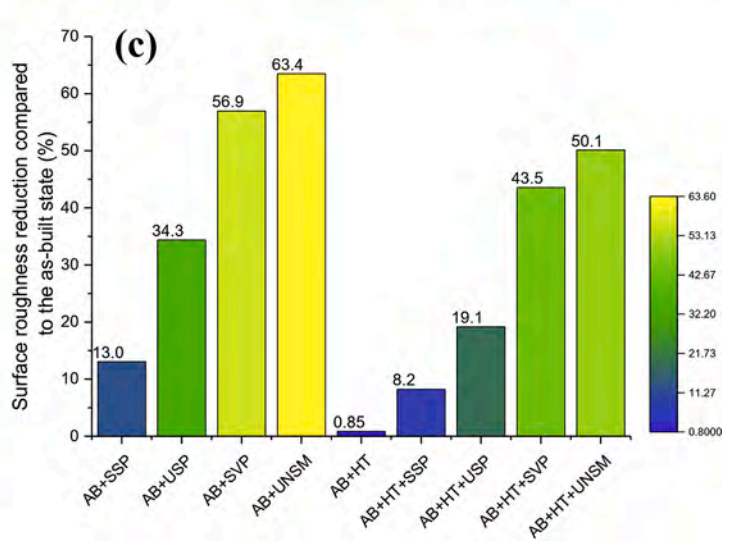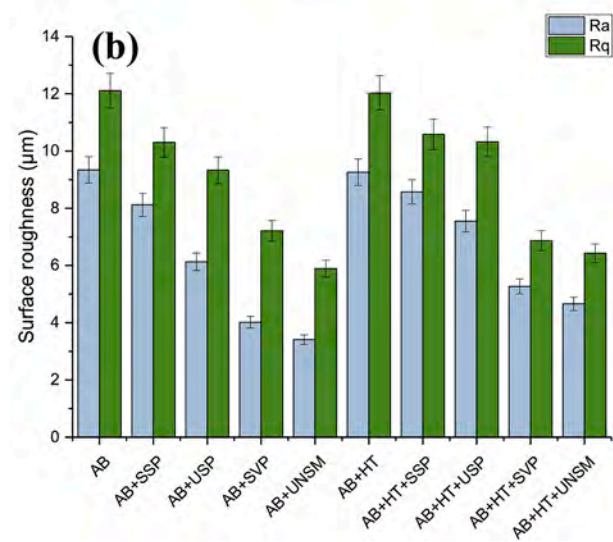
Fig. 10. (a) Surface morphologies of specimens using SEM and confocal observations, (b) calculated surface roughness parameters R_a and R_q, and (c) comparison of the effects of all post-processing methods on roughness reduction compared to initial state (based on R_a values).
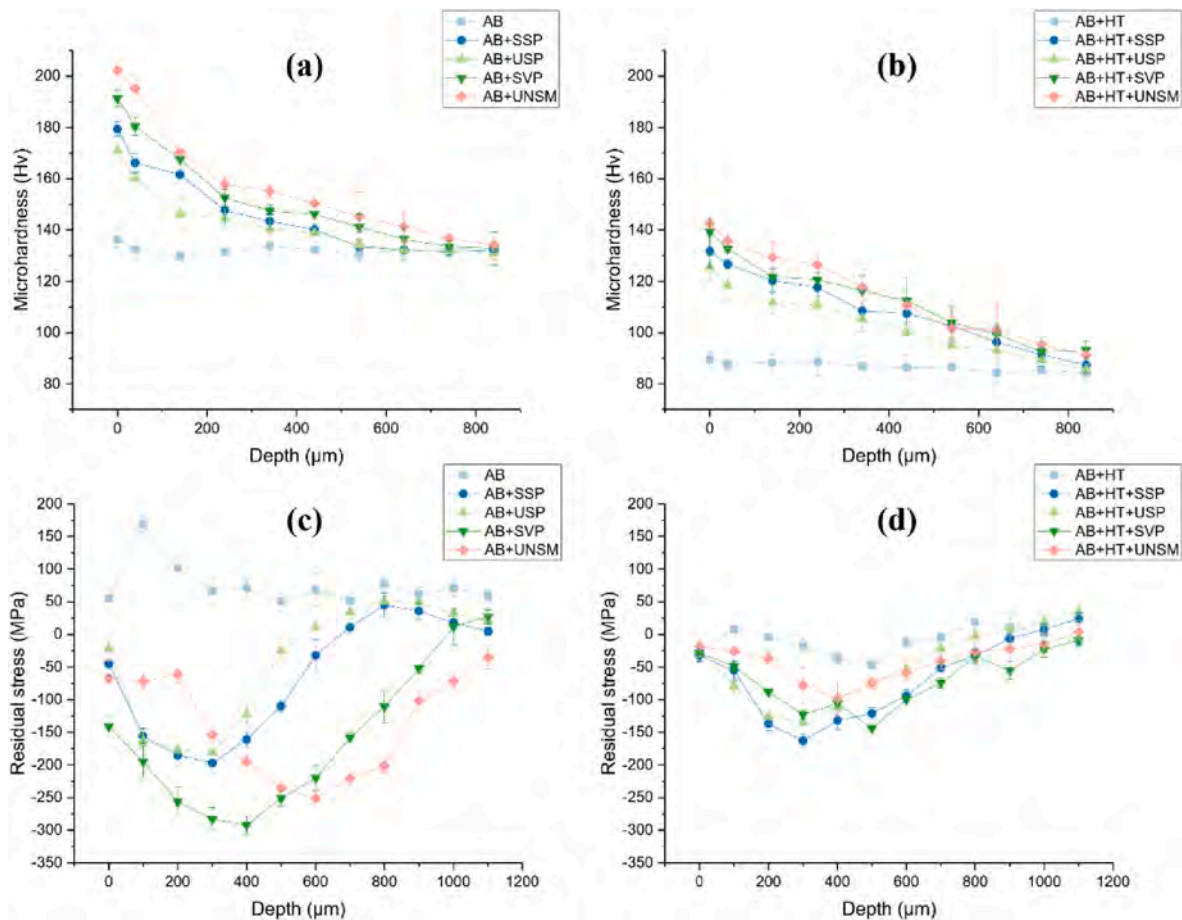
Fig. 11. Microhardness profiles for surface treated specimens with initial (a) AB and (b) AB + HT states, and distributions of residual stresses for surface treated specimens with initial (c) AB and (d) AB + HT states.

the most effective on refining the grains followed by SVP, SSP and USP. Moreover, as presented in Fig. 6b, specimens treated with UNSM achieved the highest fraction of plastically deformed grain intensity per unit area followed by SVP, SSP and USP.

XRD analyses were also used for the determination of top surface crystallite size employing Williamson-Hall methods. Fig. 7a presents the XRD patterns of all the conditions. The applied mechanical surface post-treatments diminished the peak intensity and caused peak-broadening and shift owing to the severe plastic deformation. Fig. 7b indicates that the calculated top surface crystallites size of the surface treated specimens is lower than 100 nm. In particular, surface crystallites size of 32, 36, 25,19, 52, 60, 44 and 28 nm were measured after AB + SSP, AB + USP, AB + SVP, AB + UNSM, AB + HT + SSP, AB + HT + USP, AB + HT + SVP and AB + HT + UNSM operations, respectively. The UNSM treatment had the highest influence on top surface nanocrystallization thereafter SVP, SSP and USP, while all these treatments were implemented using the same intensity of 10–12 A [0.001 inch]. The micro-strains for the specimens are demonstrated in Fig. 7c showing considerable plastic strain induced by the mechanical surface treatments. Moreover, it was found that trends of variations of grains size and plastic strains obtained by XRD agree with the ones obtained for grains size by KAM and strain contouring maps from EBSD analysis (see Figs. 5 and 6a).

In the previous works on the effects of SVP on microstructural evolution and fatigue performance of V-notched LPBF AlSi10Mg [37], we reported that besides the formation of gradient microstructure caused by grain refinement, a chemical gradient of Si phase was also observed. Herein, to investigate this phenomenon, EDS analysis was performed on the surface as depicted in Fig. 8a. Two spectrum points were considered

in each specimen. EDS maps were obtained in the same area used for EBSD analyses (30 × 150 μm^2), adding one spectrum point on the outmost deformed surface and another one in the sub-surface area, i.e. 130 μm below the surface. The results reveal that the fraction of Al phase was reduced after surface treatments while Si phase fraction increased on the outmost zone. In addition, the fibrous Si networks observed in the AB state were transformed to homogeneously dispersed spherical Si particles after HT. This considerable increase of Si fraction on the outmost surface is quantitatively demonstrated in Fig. 8b and c.

In the top surfaces, Si fractions of 34.2, 28.6, 38.7, 40.1, 21.4, 15.7, 27.1 and 31.7% resulted from AB + SSP, AB + USP, AB + SVP, AB + UNSM, AB + HT + SSP, AB + HT + USP, AB + HT + SVP and AB + HT + UNSM operations, respectively. However, in the sub-surface regions, the Si fractions were only 7.3–15.1 and 5.7–9.4% for plastically deformed specimens with initial AB and HT conditions, respectively. The results indicate the occurrence of Si phase chemical gradient near the surface zone. The amount and distribution of Si content can considerably impact the tensile strength and tribological features of Al–Si alloys [90,91]. Increasing the content of Si in Al alloy can enhance the hardenability, which typically leads to reduced EL [92]. It has been shown that by increasing the content of Si in LPBF Al–Si alloys, the solidification cracking risk can be decreased [93] and tensile strength can be improved [94]. Therefore, application of these surface treatments can enhance performance and local strengthening through simultaneous induction of microstructural (confirmed by EBSD analyses) and chemical (confirmed by EDS analyses) gradients.
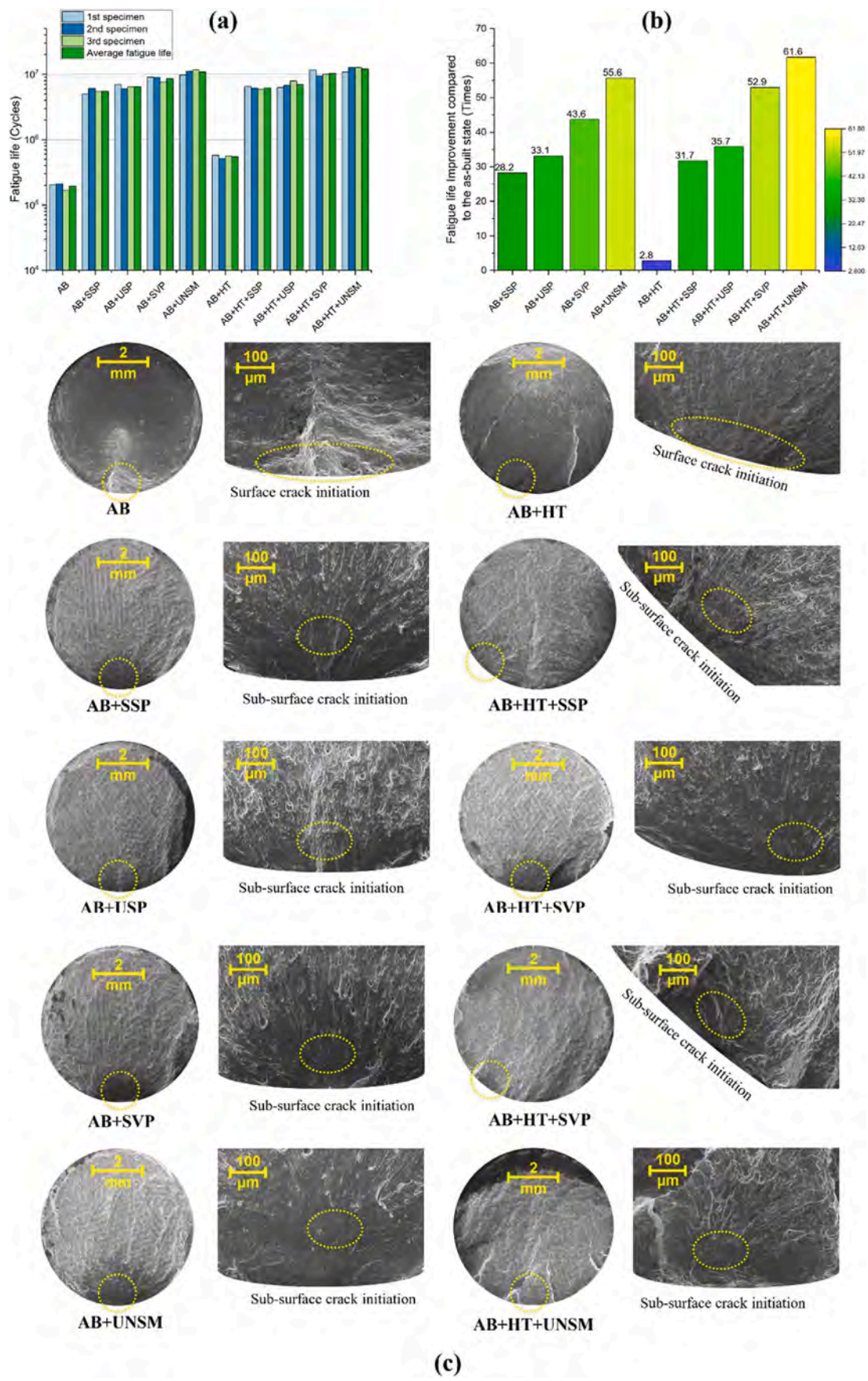
Fig. 12. (a) Fatigue test results at a stress of 110 MPa, (b) fatigue life alteration of post-processed specimens compared to the AB ones and (c) fracture surfaces specifying crack nucleation site and crack propagation direction.

3.3. Porosity analysis

Fig. 9a indicates the scanned area using X-ray computed tomography for porosity measurement on the mid-part of the specimens. The narrowest section of specimens was selected as it theoretically should be the most critical section prone to fatigue failure. Three different specimens were employed for porosity analysis of each condition. Fig. 9b shows the micro-CT images of the specimens in which the heterogeneously distributed pores can be distinguished with black color. The micro-CT images reveal that porosity was reduced by the mechanical surface treatments. Considering all the scanning area, mean porosities of 0.61, 0.39, 0.43, 0.28, 0.21, 0.57, 0.31, 0.38, 0.21 and 0.16% were measured for AB, AB + SSP, AB + USP, AB + SVP, AB + UNSM, AB + HT, AB + HT + SSP, AB + HT + USP, AB + HT + SVP and AB + HT + UNSM specimens, respectively (see Fig. 9c).

In addition, most of the sub-surface porosities were closed in the mechanically treated specimens; however, within different depths. As shown in Fig. 9d, depths of pore closure from surface were measured to be 155, 141, 194, 247, 169, 151, 221 and 278 μm after AB + SSP, AB + USP, AB + SVP, AB + UNSM, AB + HT + SSP, AB + HT + USP, AB + HT + SVP and AB + HT + UNSM operations, respectively. UNSM exhibited the highest efficacy for pore closure, followed by SVP, SSP and USP, respectively. Overall, the depth of pores closure was higher in the HT series due to their lower strength, resulting in deeper effect of mechanical surface treatment, compared to the specimens in AB initial condition.

3.4. Surface roughness and morphology analysis

The SEM and confocal surface morphological observations of all specimens are presented in Fig. 10a. Due to the attached unmelted/partially melted powders, the surface of both AB/AB + HT specimens were considerably rough. However, these powder particles were removed after the application of peening-based treatments leading to more uniform surface morphologies. Due to the physics of the surface operations and the specifics of the corresponding apparatus, each method created a unique surface morphology. In the case of SSP, USP and SVP treatments, the impact of shots created dimples and overlapping craters, with different depth and shapes due to the differences in the used media for each treatment. Nevertheless, the UNSM treated specimens exhibited a totally different surface morphology with semi-parallel tracks indicating the scanning directions.

The roughness parameters of R_a and R_q are presented in Fig. 10b for each surface treatment condition. The results reveal that R_a values of both AB/AB + HT specimens with 9.34 and 9.26 μm, respectively, were decreased after mechanical surface treatments down to 8.12, 6.13, 4.02, 3.41, 9.26, 8.57, 7.55, 5.27 and 4.66 μm for AB + SSP, AB + USP, AB + SVP, AB + UNSME, AB + HT + SSP, AB + HT + USP, AB + HT + SVP and AB + HT + UNSM specimens, respectively. Roughness of the surface treated specimens in the non-HT state were generally lower than the ones in heat treated condition. The phenomena could be clarified via higher deformability of HT specimens allowing the mechanical treatments to induce deeper surface deformation. R_q values exhibited a similar trend with R_a. Fig. 10c shows the effectiveness of the post-processing methods on surface roughness reduction by comparing their resulting R_a to the initial untreated specimens. UNSM was the most influential operation on surface texture followed by SVP, USP and SSP. Although SSP induced higher plastic strains compared to USP (according to the obtained results of microstructural characterization in section 3.2 and porosity analyses in section 3.3), surface morphology images reveal a more uniform surface after USP. In addition, it was found that USP can be more effective than SSP in surface roughness reduction. Similar results were reported comparing the application of USP and SP processes with almost same intensities on LPBF Ti–6Al–4V [95]. The phenomenon is due to the intrinsic differences between the two treatments.

3.5. Microhardness and residual stress measurement

The near surface microhardness profiles of specimens in non-HT and HT conditions are presented in Fig. 11a and b, respectively. AB + HT specimens, with higher ductility and lower strength, exhibit lower microhardness compared to the AB ones [58]. The surface treatments led to considerable surface layer hardening with the highest micro-hardness on the outmost surface that steadily decreases towards the center of the specimen. Grain size reduction is well known to induce strengthening [96]. Considering grain refinement data obtained from the EBSD analysis, as expected UNSM exhibited the highest surface hardness followed by SVP, SSP and USP. Surface microhardness improvements of 31, 25, 40, 48, 47, 40, 56 and 59% were accomplished for AB + SSP, AB + USP, AB + SVP, AB + UNSME, AB + HT + SSP, AB + HT + USP, AB + HT + SVP and AB + HT + UNSM specimens, respectively. As results indicate, higher hardness improvement was obtained in HT specimens owing to their higher deformability.

The residual stress distributions from the outmost layer towards the inside of the specimens for all conditions are presented in Fig. 11c and d. TRS in the AB specimens were released and transformed to CRS in the AB + HT specimens. Mechanical surface post-treatments remarkably induced CRS in the specimens in both AB and HT initial condition. The trend of the induced CRS varied based on the applied surface treatment. Surface residual stresses of 55, -45, −21, −141, −67, −25, −32, −24, −28 and −18 were measured for AB, AB + SSP, AB + USP, AB + SVP, AB + UNSME, AB + HT, AB + HT + SSP, AB + HT + USP, AB + HT + SVP and AB + HT + UNSM conditions, respectively. Among surface treated specimens that were initially non-HT, the highest maximum CRS was obtained for the AB + SVP specimens (−292 MPa) and the highest depth of CRS was achieved in AB + UNSM specimens (1100 μm).

3.6. Fatigue behavior

Rotating bending fatigue experiments at stress level of 110 MPa were conducted using 3 specimens per set to assess the fatigue behavior of LPBF AlSi10Mg as affected by post-processing. Fig. 12a presents the results of fatigue tests confirming that all the individual and hybrid post-treatments positively impact the fatigue performance of the hourglass LPBF AlSi10Mg specimens. Fatigue lives improved after applying HT because of microstructural homogenization, enhanced ductility, and relaxation of the TRS. From another perspective, mechanical surface treatments enhanced the fatigue performance resulting from the combined effects of considerable pore closure just below the surface, surface grain refinement and hardening, induced CRS and surface texture reduction. The hybrid post-processing methods (HT + surface treatments) take advantage of all the above-mentioned effects in a synergistic manner.

Mean fatigue lives of 1.95×10^5, 5.51×10^6, 6.47×10^6, 8.53×10^6, 1.08×10^7, 5.5×10^5, 6.19×10^6, 6.98×10^6, 1.03×10^7 and 1.20×10^7 cycles were obtained for AB, AB + SSP, AB + USP, AB + SVP, AB + UNSM, AB + HT, AB + HT + SSP, AB + HT + USP, AB + HT + SVP and AB + HT + UNSM conditions, respectively. The results exhibited noteworthy fatigue life improvement particularly in HT + UNSM, HT + SVP and UNSM processes with over 10^7 cycles. Fig. 12b represents the corresponding fatigue life enhancement by post-processing in comparison with the AB condition. UNSM demonstrated higher fatigue resistance than SVP, USP and SSP operations for both AB and AB + HT conditions. The results indicate that while SSP treated specimens had higher hardness and CRS as well as more porosity reduction compared to the SVP treated ones, the SVP sets exhibited higher fatigue lives highlighting substantial effect of lower surface roughness and morphology regularity.

Fatigue fracture surfaces are shown in Fig. 12c. The crack initiated from surface and propagated in the bulk in both AB and AB + HT specimens. Nevertheless, in the specimens subjected to mechanical surface treatments (in both initially AB and AB + HT states), sub-surface crack initiations were observed resulting from surface roughness
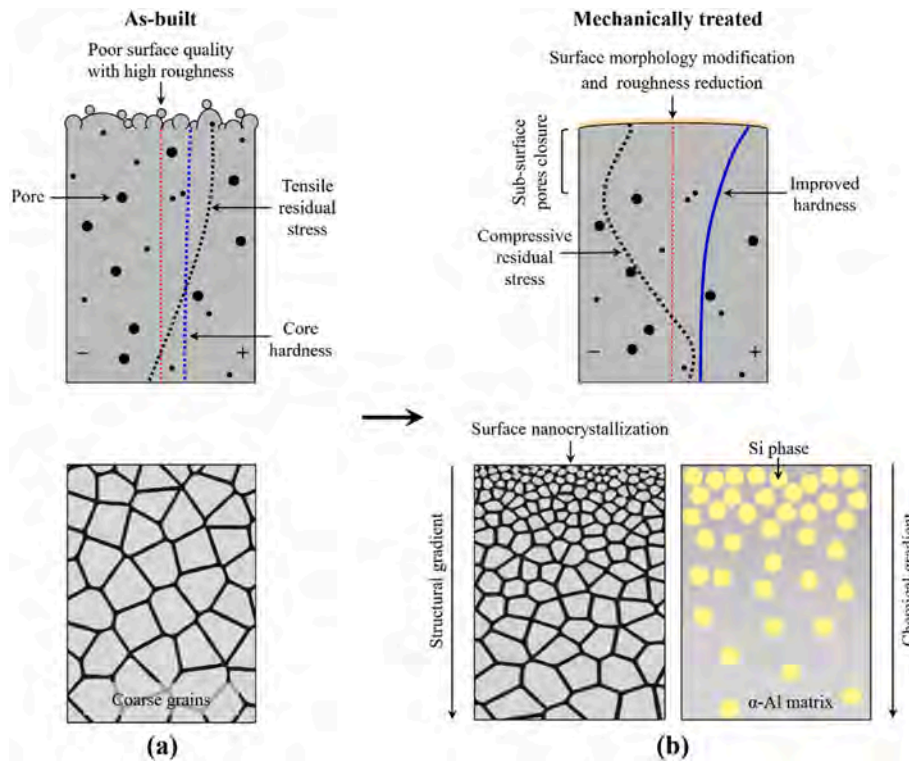
Fig. 13. Schematic illustration of the (a) AB specimen with internal and surface defects compared to the (b) specimen subjected to mechanical surface treatments with modified properties.

reduction, as well as surface layer hardening and CRS.

4. Discussions

According to the obtained results it was found that applying post-processing methods can highly modify the internal and surface anomalies of LPBF AlSi10Mg specimen compared to the as-built state. Fig. 13 schematically illustrates the near-surface state of AB specimens with the intrinsic internal and surface anomalies compared to the specimens subjected to mechanical surface treatments. These surface post-processing methods induced gradients in microstructure and chemical composition on the surface, resulting from the formation of nanosized grains and promoting the density of Si particles. UNSM showed the best performance on surface nanocrystallization, formation of structural and chemical gradients, inducing plastic strains and surface layer hardening followed by SVP, SSP and USSP. Formation of gradients in surface layer led to improved hardness and strength, induce CRS and sub-surface pore

closure, while at the same time enhance the surface morphology and reduce surface texture. In addition, mechanical surface treatments were effective in inducing sub-surface pore closure and compressive residual stresses. A maximum depth of pore closure of 278 μm was obtained through the hybrid post-treatment of HT + UNSM. Also, the deepest compressive residual stresses were achieved with UNSM (up to the depth 1100 μm).

UNSM demonstrated highest efficiency for improved fatigue behavior followed by SVP, USP and SSP operations, respectively, for both as-built and heat treated conditions. In addition, the results revealed that the effective parameters of relative density, depth of pore closure, surface layer grain refinement and hardening, residual stress distributions and surface texture as well tensile properties, all together simultaneously affect the fatigue behavior but with different impacts. For instance, the results indicate that while SSP treated specimens had higher hardness and CRS as well as more porosity reduction compared to the USP treated series, the USP sets exhibited higher fatigue lives
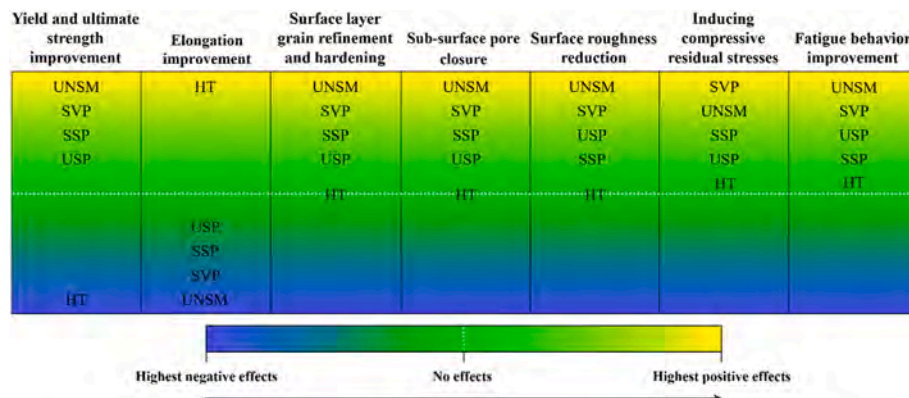
Fig. 14. Comparison of the effect of post-processing methods on YS and UTS, ductility, grain refinement and hardening, roughness, CRS, and fatigue performance.

Fig. 15. Rating variables using five levels and associated scores for (a) Time-Money, (b) Cost-Performance outputs and (c) obtained scores of considered post-processing methods by means of cost/performance analysis, as well as overall ranks based on the results of Cost-Performance analyses by considering priority for (d) performance and (e) cost.

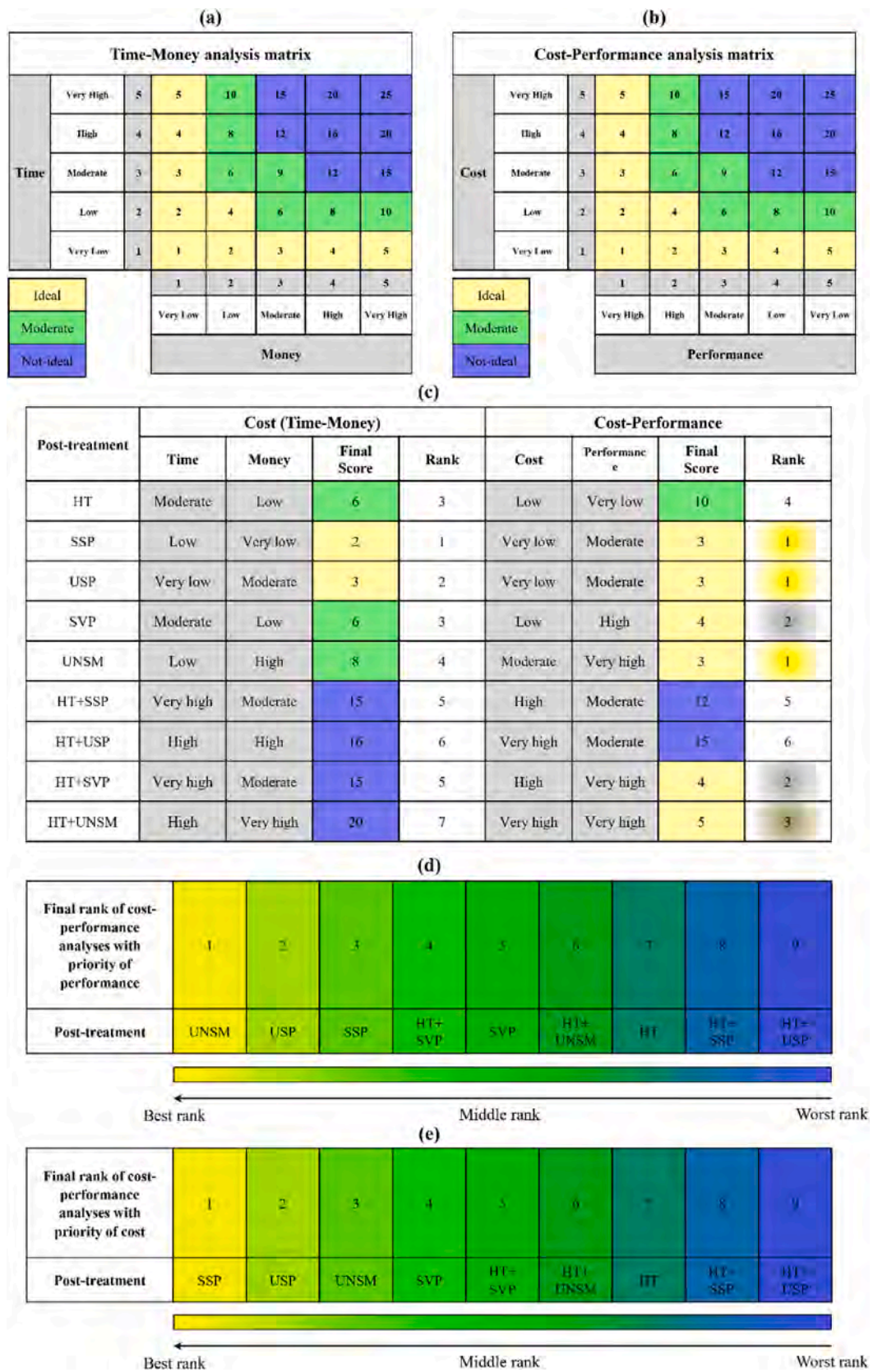highlighting substantial effect of lower surface roughness and regular morphology. The influence of each post-processing method individually on YS and UTS, ductility, grain refinement and hardening, pore closure, surface texture modification and CRS and finally fatigue performance of the post-treated specimens are summarized in Fig. 14.

Moreover, in order to compare the performance of applied post-treatments in economical fashion, Cost analysis and Cost-Performance analysis were carried out to determine the efficiency of the post-operations, particularly in terms of fatigue performance improvement. Following the methods used in risk analysis [97,98], each input was assessed as five levels of quite (very) low, low, moderate, high and quite (very) high with progressive scores of 1–5. Subsequently, a matrix was used for each set of data (Time-Money or Cost-Performance) to calculate scores for the post-operations [99]. The developed matrices of duration (Time)-Money and Cost-Performance relations are shown in Fig. 15a and b, respectively. The scores and ranks of cost (Time-Money) analysis were used in the Cost-Performance analysis. The determined scores for post-processing methods and the evaluated final ranks are shown in Fig. 15c. The criteria of assigning levels to time (considering required time for treatment of 15 specimens) and performance parameters are presented in Appendix A. The comparative cost and time levels related to each treatment were determined based on the authors' experience. The analysis results indicate similar rankings for some of the treatments regarding both cost and performance related factors. Considering the priorities of performance and cost, the applied post-treatments can be ranked as depicted in Fig. 15d and e, respectively. For instance, by considering the priority of performance in the Cost-Performance analyses, UNSM was found as the first rank treatment followed by USP, SSP, HT + SVP, SVP, HT + UNSM, HT, HT + SSP and HT + USP.

5. Conclusions

In this study, the efficacy of various mechanical surface post-treatments, involving SSP, USSP, SVP and UNSM, independent of and combined with T6 type heat treatment, was investigated on reducing the hazardous influence of internal and external (surface) imperfections on fatigue performance of LPBF AlSi10Mg specimens. Based on the experimental observations and analysis of the results, the following conclusions can be drawn:

- The mechanical surface treatments induced maximum of 0.5% reduction of elongation, while improving the yield and ultimate tensile strengths up by 21 and 15%, respectively, owing to grain size reduction and compressive residual stresses.
- While each mechanical surface treatment generated a distinct surface morphology, all of them eliminated the surface imperfections and reduced the surface roughness leading to a more uniform surface morphology. Contrary to all surface treatments that generated overlapping surface dimples due to impacting of shots with different depths and shapes of valleys, UNSM induced semi-parallel lines along scanning directions. UNSM was found to be the most influential technique in surface roughness reduction, followed by SVP, USP and SSP, in order.
- In general, all the employed mechanical surface treatments improved the fatigue performance due to their remarkable synergistic effect of increasing tensile strength, inducing pore closure, reducing the surface grain size, increasing the surface hardening, and inducing compressive residual stresses in addition to surface texture reduction. The best fatigue life enhancement was obtained for the hybrid treatments; heat treatment + UNSM ($\times$ 61) followed by UNSM ($\times$ 55) and heat treatment + SVP ($\times$ 52) compared to the AB condition.
- Obtained results of Cost-Performance analyses by considering parameters of time, cost and performance with a special focus on fatigue behavior identified UNSM as the first-rank treatment followed by USP, SVP, HT + SVP, SVP, HT + UNSM, HT, HT + SSP and HT + USP. However, it should be noted that the selection of a proper shot-processing treatment for additively manufactured parts requires a case-by-case study in which the effect of geometry and material properties should be also considered.

CRediT authorship contribution statement

Erfan Maleki: Conceptualization, Investigation, Formal analysis, Visualization, Writing – original draft. **Sara Bagherifard:** Conceptualization, Methodology, Validation, Writing – review & editing, Supervision. **Okan Unal:** Methodology, Investigation, Formal analysis, Writing – review & editing. **Shuai Shao:** Formal analysis, Writing – review & editing. **Nima Shamsaei:** Resources, Writing – review & editing. **Mario Guagliano:** Conceptualization, Resources, Writing – review & editing, Supervision.

Declaration of competing interest

The authors declare that they have no known competing financial interests or personal relationships that could have appeared to influence the work reported in this paper.

Data availability

Data will be made available on request.

Acknowledgment

Appendix A

Table A1
Time intervals considered for assigning time levels

Time level	Very low	Low	Moderate	High	Very high
Time interval (min)	0–199	200–399	400–599	600–799	800–1000

Table A2

Fatigue life improvement intervals considered for assigning performance levels

Performance level	Very low	Low	Moderate	High	Very high
Fatigue life improvement (times)	0–12.3	12.4–24.7	24.8–37.1	37.2–49.5	49.6–62

Table A3

Assigned levels of time and performance for all the applied post-treatments

Post-treatment	Required time for treatment of 1 sample (min)	Required time for treatment of 15 samples (min)	Time level	Fatigue life improvement (times)	Performance level
HT	550	550	Moderate	2.8	Very low
SSP	25	25 × 15 = 375	Low	28.2	Moderate
USP	5	5 × 15 = 75	Very low	33.1	Moderate
SVP	30	30 × 15 = 450	Moderate	43.6	High
UNSM	15	15 × 15 = 225	Low	55.6	Very high
HT + SSP	550 + 25	550+(25 × 15) = 925	Very high	31.7	Moderate
HT + USP	550 + 5	550+(5 × 15) = 625	High	35.7	Moderate
HT + SVP	550 + 30	550+(30 × 15) = 1000	Very high	52.9	Very high
HT + UNSM	550 + 15	550+(15 × 15) = 775	High	61.6	Very high

References

[1] X. Liu, C. Zhao, X. Zhou, Z. Shen, W. Liu, Microstructure of selective laser melted AlSi10Mg alloy, Mater. Des. 168 (2019), 107677, https://doi.org/10.1016/j.matdes.2019.107677.

[2] M. Tang, P.C. Pistorius, S. Narra, J.L. Beuth, Rapid solidification: selective laser melting of AlSi10Mg, JOM (J. Occup. Med.) 68 (2016) 960–966, https://doi.org/10.1007/s11837-015-1763-3.

[3] I. Yadroitsev, I. Smurov, Surface morphology in selective laser melting of metal powders, Phys. Procedia (2011) 264–270, https://doi.org/10.1016/j.phpro.2011.03.034.

[4] E. Maleki, S. Bagherifard, M. Guagliano, Application of artificial intelligence to optimize the process parameters effects on tensile properties of Ti-6Al-4V fabricated by laser powder-bed fusion, Int. J. Mech. Mater. Des. 18 (2022) 199–222, https://doi.org/10.1007/s10999-021-09570-w.

[5] J.W. Pegues, S. Shao, N. Shamsaei, N. Sanaei, A. Fatemi, D.H. Warner, P. Li, N. Phan, Fatigue of additive manufactured Ti-6Al-4V, Part I: the effects of powder feedstock, manufacturing, and post-process conditions on the resulting microstructure and defects, Int. J. Fatig. 132 (2020), https://doi.org/10.1016/j.ijfatigue.2019.105358.

[6] D. Herzog, V. Seyda, E. Wycisk, C. Emmelmann, Additive manufacturing of metals, Acta Mater. 117 (2016) 371–392, https://doi.org/10.1016/j.actamat.2016.07.019.

[7] P. Ferro, A. Fabrizi, F. Berto, G. Savio, R. Meneghello, S. Rosso, Defects as a root cause of fatigue weakening of additively manufactured AlSi10Mg components, Theor. Appl. Fract. Mech. 108 (2020), 102611, https://doi.org/10.1016/j.tafmec.2020.102611.

[8] N.T. Aboulkhair, N.M. Everitt, I. Ashcroft, C. Tuck, Reducing porosity in AlSi10Mg parts processed by selective laser melting, Addit. Manuf. 1 (2014) 77–86, https://doi.org/10.1016/j.addma.2014.08.001.

[9] B.J. Mfusi, N.R. Mathe, L.C. Tshabalala, P.A.I. Popoola, The effect of stress relief on the mechanical and fatigue properties of additively manufactured AlSi10Mg parts, Metals 9 (2019), https://doi.org/10.3390/met9111216.

[10] T. Mukherjee, W. Zhang, T. DebRoy, An improved prediction of residual stresses and distortion in additive manufacturing, Comput. Mater. Sci. 126 (2017) 360–372, https://doi.org/10.1016/j.commatsci.2016.10.003.

[11] M.H. Nasab, D. Gastaldi, N.F. Lecis, M. Vedani, On morphological surface features of the parts printed by selective laser melting (SLM), Addit. Manuf. 24 (2018) 373–377, https://doi.org/10.1016/j.addma.2018.10.011.

[12] W.J. Sames, F.A. List, S. Pannala, R.R. Dehoff, S.S. Babu, The metallurgy and processing science of metal additive manufacturing, Int. Mater. Rev. 61 (2016) 315–360, https://doi.org/10.1080/09506608.2015.1116649.

[13] Z. Zhang, C. Sun, X. Xu, L. Liu, Surface quality and forming characteristics of thin-wall aluminium alloy parts manufactured by laser assisted MIG arc additive manufacturing, Int. J. Light. Mater. Manuf. 1 (2018) 89–95, https://doi.org/10.1016/j.ijlmm.2018.03.005.

[14] R. Li, J. Liu, Y. Shi, L. Wang, W. Jiang, Balling behavior of stainless steel and nickel powder during selective laser melting process, Int. J. Adv. Manuf. Technol. 59 (2012) 1025–1035, https://doi.org/10.1007/s00170-011-3566-1.

[15] A. Fatemi, R. Molaei, J. Simsiriwong, N. Sanaei, J. Pegues, B. Torries, N. Phan, N. Shamsaei, Fatigue behaviour of additive manufactured materials: an overview of some recent experimental studies on Ti-6Al-4V considering various processing and loading direction effects, Fatig. Fract. Eng. Mater. Struct. 42 (2019) 991–1009, https://doi.org/10.1111/ffe.13000.

[16] Z. Xu, A. Liu, X. Wang, Fatigue performance and crack propagation behavior of selective laser melted AlSi10Mg in 0°, 15°, 45° and 90° building directions, Mater. Sci. Eng. A 812 (2021), https://doi.org/10.1016/j.msea.2021.141141.

[17] S. Beretta, M. Gargourimotlagh, S. Foletti, A. du Plessis, M. Riccio, Fatigue strength assessment of "as built" AlSi10Mg manufactured by SLM with different build orientations, Int. J. Fatig. 139 (2020), https://doi.org/10.1016/j.ijfatigue.2020.105737.

[18] E. Maleki, S. Bagherifard, O. Unal, F. Sabouri, M. Bandini, M. Guagliano, Effects of different mechanical and chemical surface post-treatments on mechanical and surface properties of as-built laser powder bed fusion AlSi10Mg, Surf. Coating. Technol. 439 (2022), 128391, https://doi.org/10.1016/j.surfcoat.2022.128391.

[19] A. Yadollahi, N. Shamsaei, Additive manufacturing of fatigue resistant materials: challenges and opportunities, Int. J. Fatig. 98 (2017) 14–31, https://doi.org/10.1016/j.ijfatigue.2017.01.001.

[20] S. Lee, J.W. Pegues, N. Shamsaei, Fatigue behavior and modeling for additive manufactured 304L stainless steel: the effect of surface roughness, Int. J. Fatig. (2020), https://doi.org/10.1016/j.ijfatigue.2020.105856.

[21] J.W. Pegues, N. Shamsaei, M.D. Roach, R.S. Williamson, Fatigue life estimation of additive manufactured parts in the as-built surface condition, Mater. Des. Process. Commun. (2019), https://doi.org/10.1002/mdp2.36.

[22] A. Leon, E. Aghion, Effect of surface roughness on corrosion fatigue performance of AlSi10Mg alloy produced by Selective Laser Melting (SLM), Mater. Char. 131 (2017) 188–194, https://doi.org/10.1016/j.matchar.2017.06.029.

[23] A.R. Balachandramurthi, J. Moverare, N. Dixit, R. Pederson, Influence of defects and as-built surface roughness on fatigue properties of additively manufactured Alloy 718, Mater. Sci. Eng. A 735 (2018) 463–474, https://doi.org/10.1016/j.msea.2018.08.072.

[24] C. Ye, C. Zhang, J. Zhao, Y. Dong, Effects of post-processing on the surface finish, porosity, residual stresses, and fatigue performance of additive manufactured metals: a review, J. Mater. Eng. Perform. 30 (2021) 6407–6425, https://doi.org/10.1007/s11665-021-06021-7.

[25] E. Maleki, S. Bagherifard, M. Bandini, M. Guagliano, Surface post-treatments for metal additive manufacturing: progress, challenges, and opportunities, Addit. Manuf. 37 (2021), 101619, https://doi.org/10.1016/j.addma.2020.101619.

[26] M. Åsberg, G. Fredriksson, S. Hatami, W. Fredriksson, P. Krakhmalev, Influence of post treatment on microstructure, porosity and mechanical properties of additive manufactured H13 tool steel, Mater. Sci. Eng. A 742 (2019) 584–589, https://doi.org/10.1016/j.msea.2018.08.046.

[27] Z. Qi, B. Qi, B. Cong, H. Sun, G. Zhao, J. Ding, Microstructure and mechanical properties of wire + arc additively manufactured 2024 aluminum alloy components: as-deposited and post heat-treated, J. Manuf. Process. 40 (2019) 27–36, https://doi.org/10.1016/j.jmapro.2019.03.003.

[28] L.M.S. Santos, L.P. Borrego, J.A.M. Ferreira, J. de Jesus, J.D. Costa, C. Capela, Effect of heat treatment on the fatigue crack growth behaviour in additive manufactured AISI 18Ni300 steel, Theor. Appl. Fract. Mech. 102 (2019) 10–15, https://doi.org/10.1016/j.tafmec.2019.04.005.

[29] M. Komarasamy, S. Shukla, S. Williams, K. Kandasamy, S. Kelly, R.S. Mishra, Microstructure, fatigue, and impact toughness of additively manufactured nickel alloy 718, Addit. Manuf. 28 (2019) 661–675, https://doi.org/10.1016/j.addma.2019.06.009.

[30] A. Yegyan Kumar, Y. Bai, A. Eklund, C.B. Williams, The effects of Hot Isostatic Pressing on parts fabricated by binder jetting additive manufacturing, Addit. Manuf. 24 (2018) 115–124, https://doi.org/10.1016/j.addma.2018.09.021.

[31] M.N. Gussev, N. Sridharan, Z. Thompson, K.A. Terrani, S.S. Babu, Influence of hot isostatic pressing on the performance of aluminum alloy fabricated by ultrasonic

additive manufacturing, Scripta Mater. (2018), https://doi.org/10.1016/j.scriptamat.2017.10.004.

[32] R. Molaei, A. Fatemi, Crack paths in additive manufactured metallic materials subjected to multiaxial cyclic loads including surface roughness, HIP, and notch effects, Int. J. Fatig. (2019), https://doi.org/10.1016/j.ijfatigue.2019.03.007.

[33] M. Benedetti, V. Fontanari, M. Bandini, F. Zanini, S. Carmignato, Low- and high-cycle fatigue resistance of Ti-6Al-4V ELI additively manufactured via selective laser melting: mean stress and defect sensitivity, Int. J. Fatig. 107 (2018) 96–109, https://doi.org/10.1016/j.ijfatigue.2017.10.021.

[34] E. Salvati, A.J.G. Lunt, S. Ying, T. Sui, H.J. Zhang, C. Heason, G. Baxter, A. M. Korsunsky, Eigenstrain reconstruction of residual strains in an additively manufactured and shot peened nickel superalloy compressor blade, Comput. Methods Appl. Mech. Eng. 320 (2017) 335–351, https://doi.org/10.1016/j.cma.2017.03.005.

[35] D.A. Lesyk, V.V. Dzhemelinskyi, S. Martinez, B.N. Mordyuk, A. Lamikiz, Surface shot peening post-processing of inconel 718 alloy parts printed by laser powder bed fusion additive manufacturing, J. Mater. Eng. Perform. 30 (2021) 6982–6995, https://doi.org/10.1007/s11665-021-06103-6.

[36] N. Alharbi, Corrosion Resistance of 3D Printed SS316L Post-processed by Ultrasonic Shot Peening at Optimum Energy Level, 2022, https://doi.org/10.1177/09544054221112164.

[37] E. Maleki, S. Bagherifard, O. Unal, M. Bandini, M. Guagliano, The effects of microstructural and chemical surface gradients on fatigue performance of laser powder bed fusion AlSi10Mg, Mater. Sci. Eng. A 840 (2022), 142962, https://doi.org/10.1016/j.msea.2022.142962.

[38] R.M. Karimbaev, Y.S. Pyun, A. Amanov, Fatigue life extension of additively manufactured Nickel-base 718 alloy by nanostructured surface, Mater. Sci. Eng. A 831 (2022), 142041, https://doi.org/10.1016/j.msea.2021.142041.

[39] D.A. Lesyk, S. Martinez, B.N. Mordyuk, O.O. Pedash, V.V. Dzhemelinskyi, A. Lamikiz, Ultrasonic surface post-processing of hot isostatic pressed and heat treated superalloy parts manufactured by laser powder bed fusion, Addit. Manuf. Lett. 3 (2022), 100063, https://doi.org/10.1016/j.addlet.2022.100063.

[40] H. Zhang, J. Zhao, J. Liu, H. Qin, Z. Ren, G.L. Doll, Y. Dong, C. Ye, The effects of electrically-assisted ultrasonic nanocrystal surface modification on 3D-printed Ti-6Al-4V alloy, Addit. Manuf. (2018), https://doi.org/10.1016/j.addma.2018.04.035.

[41] Y. Efe, I. Karademir, F. Husem, E. Maleki, R. Karimbaev, A. Amanov, O. Unal, Enhancement in microstructural and mechanical performance of AA7075 aluminum alloy via severe shot peening and ultrasonic nanocrystal surface modification, Appl. Surf. Sci. 528 (2020), https://doi.org/10.1016/j.apsusc.2020.146922.

[42] J. Donoghue, A.A. Antonysamy, F. Martina, P.A. Colegrove, S.W. Williams, P. B. Prangnell, The effectiveness of combining rolling deformation with Wire-Arc Additive Manufacture on β-grain refinement and texture modification in Ti-6Al-4V, Mater. Char. 114 (2016) 103–114, https://doi.org/10.1016/j.matchar.2016.02.001.

[43] M. Sato, O. Takakuwa, M. Nakai, M. Niinomi, F. Takeo, H. Soyama, Using cavitation peening to improve the fatigue life of titanium alloy Ti-6Al-4V manufactured by electron beam melting, Mater. Sci. Appl. 7 (2016) 181–191, https://doi.org/10.4236/msa.2016.74018.

[44] A. Amanov, Effect of local treatment temperature of ultrasonic nanocrystalline surface modification on tribological behavior and corrosion resistance of stainless steel 316L produced by selective laser melting, Surf. Coating. Technol. 398 (2020), https://doi.org/10.1016/j.surfcoat.2020.126080.

[45] E. Maleki, S. Bagherifard, F. Sabouri, M. Guagliano, Effects of hybrid post-treatments on fatigue behaviour of notched LPBF AlSi10Mg: experimental and deep learning approaches, Procedia Struct. Integr. 34 (2021) 141–153, https://doi.org/10.1016/j.prostr.2021.12.021.

[46] F. Trevisan, F. Calignano, M. Lorusso, J. Pakkanen, A. Aversa, E.P. Ambrosio, M. Lombardi, P. Fino, D. Manfredi, On the selective laser melting (SLM) of the AlSi10Mg alloy: process, microstructure, and mechanical properties, Materials 10 (2017), https://doi.org/10.3390/ma10010076.

[47] W.E. Frazier, Metal additive manufacturing: a review, J. Mater. Eng. Perform. 23 (2014) 1917–1928, https://doi.org/10.1007/s11665-014-0958-z.

[48] H. Hyer, L. Zhou, S. Park, G. Gottsfritz, G. Benson, B. Tolentino, B. McWilliams, K. Cho, Y. Sohn, Understanding the laser powder bed fusion of AlSi10Mg alloy, Metallogr. Microstruct. Anal. 9 (2020) 484–502, https://doi.org/10.1007/s13632-020-00659-w.

[49] N. Read, W. Wang, K. Essa, M.M. Attallah, Selective laser melting of AlSi10Mg alloy: process optimisation and mechanical properties development, Mater. Des. 65 (2015) 417–424, https://doi.org/10.1016/j.matdes.2014.09.044.

[50] M. Muhammad, P.D. Nezhadfar, S. Thompson, A. Saharan, N. Phan, N. Shamsaei, A comparative investigation on the microstructure and mechanical properties of additively manufactured aluminum alloys, Int. J. Fatig. (2021), https://doi.org/10.1016/j.ijfatigue.2021.106165.

[51] M. Hofele, A. Roth, J. Schanz, D.K. Harrison, A.K.M. De Silva, H. Riegel, Laser polishing of laser powder bed fusion AlSi10Mg parts—influence of initial surface roughness on achievable surface quality, Mater. Sci. Appl. 12 (2021) 15–41, https://doi.org/10.4236/msa.2021.121002.

[52] A. Du Plessis, D. Glaser, H. Moller, N. Mathe, L. Tshabalala, B. Mfusi, R. Mostert, Pore closure effect of laser shock peening of additively manufactured AlSi10Mg, 3D print, Addit. Manuf. 6 (2019) 245–252, https://doi.org/10.1089/3dp.2019.0064.

[53] D. Bhaduri, P. Penchev, S. Dimov, K. Essa, L.N. Carter, C.I. Pruncu, J. Jiang, D. Pullini, On the surface integrity of additive manufactured and post-processed AlSi10Mg parts, Procedia CIRP 87 (2020) 339–344, https://doi.org/10.1016/j.procir.2020.02.093.

[54] X. Xing, X. Duan, T. Jiang, J. Wang, F. Jiang, Ultrasonic peening treatment used to improve stress corrosion resistance of AlSi10Mg components fabricated using selective laser melting, Metals 9 (2019), https://doi.org/10.3390/met9010103.

[55] M.H. Nasab, A. Giussani, D. Gastaldi, V. Tirelli, M. Vedani, Effect of surface and subsurface defects on fatigue behavior of AlSi10Mg alloy processed by laser powder bed fusion (L-PBF), Metals 9 (2019), https://doi.org/10.3390/met9101063.

[56] W. Yu, S.L. Sing, C.K. Chua, X. Tian, Influence of re-melting on surface roughness and porosity of AlSi10Mg parts fabricated by selective laser melting, J. Alloys Compd. 792 (2019) 574–581, https://doi.org/10.1016/j.jallcom.2019.04.017.

[57] N.E. Uzan, S. Ramati, R. Shneck, N. Frage, O. Yeheskel, On the effect of shot-peening on fatigue resistance of AlSi10Mg specimens fabricated by additive manufacturing using selective laser melting (AM-SLM), Addit. Manuf. 21 (2018) 458–464, https://doi.org/10.1016/j.addma.2018.03.030.

[58] S. Bagherifard, N. Beretta, S. Monti, M. Riccio, M. Bandini, M. Guagliano, On the fatigue strength enhancement of additive manufactured AlSi10Mg parts by mechanical and thermal post-processing, Mater. Des. 145 (2018) 28–41, https://doi.org/10.1016/j.matdes.2018.02.055.

[59] A.H. Maamoun, M.A. Elbestawi, S.C. Veldhuis, Influence of shot peening on alsi10mg parts fabricated by additive manufacturing, J. Manuf. Mater. Process. 2 (2018), https://doi.org/10.3390/jmmp2030040.

[60] E. Maleki, S. Bagherifard, S.M.J. Razavi, M. Riccio, M. Bandini, A. du Plessis, F. Berto, M. Guagliano, Fatigue behaviour of notched laser powder bed fusion AlSi10Mg after thermal and mechanical surface post-processing, Mater. Sci. Eng. A 829 (2022), 142145, https://doi.org/10.1016/j.msea.2021.142145.

[61] E. Maleki, S. Bagherifard, F. Sabouri, M. Bandini, M. Guagliano, Hybrid thermal, mechanical and chemical surface post-treatments for improved fatigue behavior of laser powder bed fusion AlSi10Mg notched samples, Surf. Coating. Technol. 430 (2022), https://doi.org/10.1016/j.surfcoat.2021.127962.

[62] E. Maleki, S. Bagherifard, O. Unal, M. Bandini, M. Guagliano, On the effects of laser shock peening on fatigue behavior of V-notched AlSi10Mg manufactured by laser powder bed fusion, Int. J. Fatig. 163 (2022), 107035, https://doi.org/10.1016/j.ijfatigue.2022.107035.

[63] P. Costa, G. Altamirano, A. Salinas, D.S. González-González, F. Goodwin, Optimization of the continuous galvanizing heat treatment process in ultra-high strength dual phase steels using a multivariate model, Metals 9 (2019), https://doi.org/10.3390/met9060703.

[64] S. Mustapha, M.M. Ndamitso, A.S. Abdulkareem, J.O. Tijani, D.T. Shuaib, A. K. Mohammed, A. Sumaila, Comparative study of crystallite size using Williamson-Hall and Debye-Scherrer plots for ZnO nanoparticles, Adv. Nat. Sci. Nanosci. Nanotechnol. 10 (2019), https://doi.org/10.1088/2043-6254/ab52f7.

[65] International Organization for Standardization, ISO 25178-2: Geometrical Product Specifications (GPS) - Surface Texture: Areal Part - 2: Terms, Definitions and Surface Texture Parameters, 2007.

[66] A. Amanov, R. Umarov, T. Amanov, Increase in strength and fretting resistance of Alloy 718 using the surface modification process, Materials 11 (2018) 1–13, https://doi.org/10.3390/ma11081366.

[67] Y. Li, Z. Lu, T. Li, D. Li, J. Lu, P.K. Liaw, Y. Zou, Effects of surface severe plastic deformation on the mechanical behavior of 304 stainless steel, Metals 10 (2020) 1–13, https://doi.org/10.3390/met10060831.

[68] Q.Q. Duan, B. Wang, P. Zhang, K. Yang, Z.F. Zhang, Improvement of notch fatigue properties of ultra-high CM400 maraging steel through shot peening, J. Mater. Res. 32 (2017) 4424–4432, https://doi.org/10.1557/jmr.2017.358.

[69] T. Rautio, M. Jaskari, T. Gundgire, T. Iso-Junno, M. Vippola, A. Järvenpää, The effect of severe shot peening on fatigue life of laser powder bed fusion manufactured 316L stainless steel, Materials 15 (2022) 1–13, https://doi.org/10.3390/ma15103517.

[70] M. Balbaa, A. Ghasemi, E. Fereiduni, K. Al-Rubaie, M. Elbestawi, Improvement of fatigue performance of laser powder bed fusion fabricated IN625 and IN718 superalloys via shot peening, J. Mater. Process. Technol. 304 (2022), 117571, https://doi.org/10.1016/j.jmatprotec.2022.117571.

[71] J.H. Moon, S.M. Baek, S.G.S. Lee, Y. Seong, A. Amanov, S.G.S. Lee, H.S. Kim, Effects of residual stress on the mechanical properties of copper processed using ultrasonic-nanocrystalline surface modification, Mater. Res. Lett. 7 (2019) 97–102, https://doi.org/10.1080/21663831.2018.1560370.

[72] P. Yang, M.A. Rodriguez, L.A. Deibler, B.H. Jared, J. Griego, A. Kilgo, A. Allen, D. K. Stefan, Effect of thermal annealing on microstructure evolution and mechanical behavior of an additive manufactured AlSi10Mg part, J. Mater. Res. 33 (2018) 1701–1712, https://doi.org/10.1557/jmr.2018.82.

[73] F. Alghamdi, X. Song, A. Hadadzadeh, B. Shalchi-Amirkhiz, M. Mohammadi, M. Haghshenas, Post heat treatment of additive manufactured AlSi10Mg: on silicon morphology, texture and small-scale properties, Mater. Sci. Eng. A 783 (2020), https://doi.org/10.1016/j.msea.2020.139296.

[74] M. Liu, N. Takata, A. Suzuki, M. Kobashi, Effect of heat treatment on gradient microstructure of AlSi10Mg lattice structure manufactured by laser powder bed fusion, Materials 13 (2020), https://doi.org/10.3390/ma13112487.

[75] L. Thijs, K. Kempen, J.P. Kruth, J. Van Humbeeck, Fine-structured aluminium products with controllable texture by selective laser melting of pre-alloyed AlSi10Mg powder, Acta Mater. 61 (2013) 1809–1819, https://doi.org/10.1016/j.actamat.2012.11.052.

[76] A. Hadadzadeh, B.S. Amirkhiz, J. Li, M. Mohammadi, Columnar to equiaxed transition during direct metal laser sintering of AlSi10Mg alloy: effect of building direction, Addit. Manuf. 23 (2018) 121–131, https://doi.org/10.1016/j.addma.2018.08.001.

[77] A. Basak, S. Das, Epitaxy and microstructure evolution in metal additive manufacturing, Annu. Rev. Mater. Res. 46 (2016) 125–149, https://doi.org/10.1146/annurev-matsci-070115-031728.

[78] A. Yadollahi, N. Shamsaei, S.M. Thompson, D.W. Seely, Effects of process time interval and heat treatment on the mechanical and microstructural properties of direct laser deposited 316L stainless steel, Mater. Sci. Eng. A 644 (2015) 171–183, https://doi.org/10.1016/j.msea.2015.07.056.

[79] U. Tradowsky, J. White, R.M. Ward, N. Read, W. Reimers, M.M. Attallah, Selective laser melting of AlSi10Mg: influence of post-processing on the microstructural and tensile properties development, Mater. Des. 105 (2016) 212–222, https://doi.org/10.1016/j.matdes.2016.05.066.

[80] B. Amir, S. Samuha, O. Sadot, Influence of selective laser melting machine source on the dynamic properties of AlSi10Mg Alloy, Materials 12 (2019) 8–12, https://doi.org/10.3390/ma12071143.

[81] W.H. Kan, Y. Nadot, M. Foley, L. Ridosz, G. Proust, J.M. Cairney, Factors that affect the properties of additively-manufactured AlSi10Mg: porosity versus microstructure, Addit. Manuf. 29 (2019), 100805, https://doi.org/10.1016/j.addma.2019.100805.

[82] T. Ben Britton, S. Birosca, M. Preuss, A.J. Wilkinson, Electron backscatter diffraction study of dislocation content of a macrozone in hot-rolled Ti-6Al-4V alloy, Scripta Mater. (2010), https://doi.org/10.1016/j.scriptamat.2010.01.010.

[83] A.J. Wilkinson, T. Ben Britton, Strains, planes, and EBSD in materials science, Mater. Today (2012), https://doi.org/10.1016/S1369-7021(12)70163-3.

[84] A. Ramazani, K. Mukherjee, A. Schwedt, P. Goravanchi, U. Prahl, W. Bleck, Quantification of the effect of transformation-induced geometrically necessary dislocations on the flow-curve modelling of dual-phase steels, Int. J. Plast. 43 (2013) 128–152, https://doi.org/10.1016/j.ijplas.2012.11.003.

[85] J. Kadkhodapour, S. Schmauder, D. Raabe, S. Ziaei-Rad, U. Weber, M. Calcagnotto, Experimental and numerical study on geometrically necessary dislocations and non-homogeneous mechanical properties of the ferrite phase in dual phase steels, Acta Mater. 59 (2011) 4387–4394, https://doi.org/10.1016/j.actamat.2011.03.062.

[86] I. Bogachev, K.M. Knowles, G.J. Gibson, Deep cold rolling of single crystal nickel-based superalloy CMSX-4, Materialia (2021), https://doi.org/10.1016/j.mtla.2021.101240.

[87] X. Liang, Z. Liu, Q. Wang, B. Wang, X. Ren, Tool wear-induced microstructure evolution in localized deformation layer of machined Ti–6Al–4V, J. Mater. Sci. 55 (2020) 3636–3651, https://doi.org/10.1007/s10853-019-04214-z.

[88] A.E. Davis, J.R. Hönnige, F. Martina, P.B. Prangnell, Quantification of strain fields and grain refinement in Ti-6Al-4V inter-pass rolled wire-arc AM by EBSD misorientation analysis, Mater. Char. 170 (2020) 151–155, https://doi.org/10.1016/j.matchar.2020.110673.

[89] C. peng Liu, R. ming Ren, D. yi Liu, X. juan Zhao, C. huan Chen, An EBSD investigation on the evolution of the surface microstructure of D2 wheel steel during rolling contact fatigue, Tribol. Lett. 68 (2020), https://doi.org/10.1007/s11249-020-1277-1.

[90] C. Butler, S. Babu, R. Lundy, R. O'Reilly Meehan, J. Punch, N. Jeffers, Effects of processing parameters and heat treatment on thermal conductivity of additively manufactured AlSi10Mg by selective laser melting, Mater. Char. 173 (2021), https://doi.org/10.1016/j.matchar.2021.110945.

[91] D.K. Dwivedi, Wear behaviour of cast hypereutectic aluminium silicon alloys, Mater. Des. 27 (2006) 610–616, https://doi.org/10.1016/j.matdes.2004.11.029.

[92] H. Torabian, J.P. Pathak, S.N. Tiwari, Wear characteristics of Al-Si alloys, Wear 172 (1994) 49–58, https://doi.org/10.1016/0043-1648(94)90298-4.

[93] D. Knoop, A. Lutz, B. Mais, A. von Hehl, A tailored ALSiMg alloy for laser powder bed fusion, Metals 10 (2020), https://doi.org/10.3390/met10040514.

[94] T. Kimura, T. Nakamoto, M. Mizuno, H. Araki, Effect of silicon content on densification, mechanical and thermal properties of Al-xSi binary alloys fabricated using selective laser melting, Mater. Sci. Eng. A 682 (2017) 593–602, https://doi.org/10.1016/j.msea.2016.11.059.

[95] Q. Zhang, S. Xu, J. Wang, X. Zhang, J. Wang, C. Si, Microstructure change and corrosion resistance of selective laser melted Ti-6Al-4V alloy subjected to pneumatic shot peening and ultrasonic shot peening, Surf. Topogr. Metrol. Prop. 10 (2022), https://doi.org/10.1088/2051-672X/ac4c83.

[96] E.O. Hall, The deformation and ageing of mild steel: III Discussion of results, Proc. Phys. Soc. B 64 (1951) 747–753, https://doi.org/10.1088/0370-1301/64/9/303.

[97] Y. Duan, J. Zhao, J. Chen, G. Bai, A risk matrix analysis method based on potential risk influence: a case study on cryogenic liquid hydrogen filling system, Process Saf. Environ. Protect. 102 (2016) 277–287, https://doi.org/10.1016/j.psep.2016.03.022.

[98] A.S. Markowski, M.S. Mannan, Fuzzy risk matrix, J. Hazard Mater. 159 (2008) 152–157, https://doi.org/10.1016/j.jhazmat.2008.03.055.

[99] L. Lu, W. Liang, L. Zhang, H. Zhang, Z. Lu, J. Shan, A comprehensive risk evaluation method for natural gas pipelines by combining a risk matrix with a bow-tie model, J. Nat. Gas Sci. Eng. 25 (2015) 124–133, https://doi.org/10.1016/j.jngse.2015.04.029.